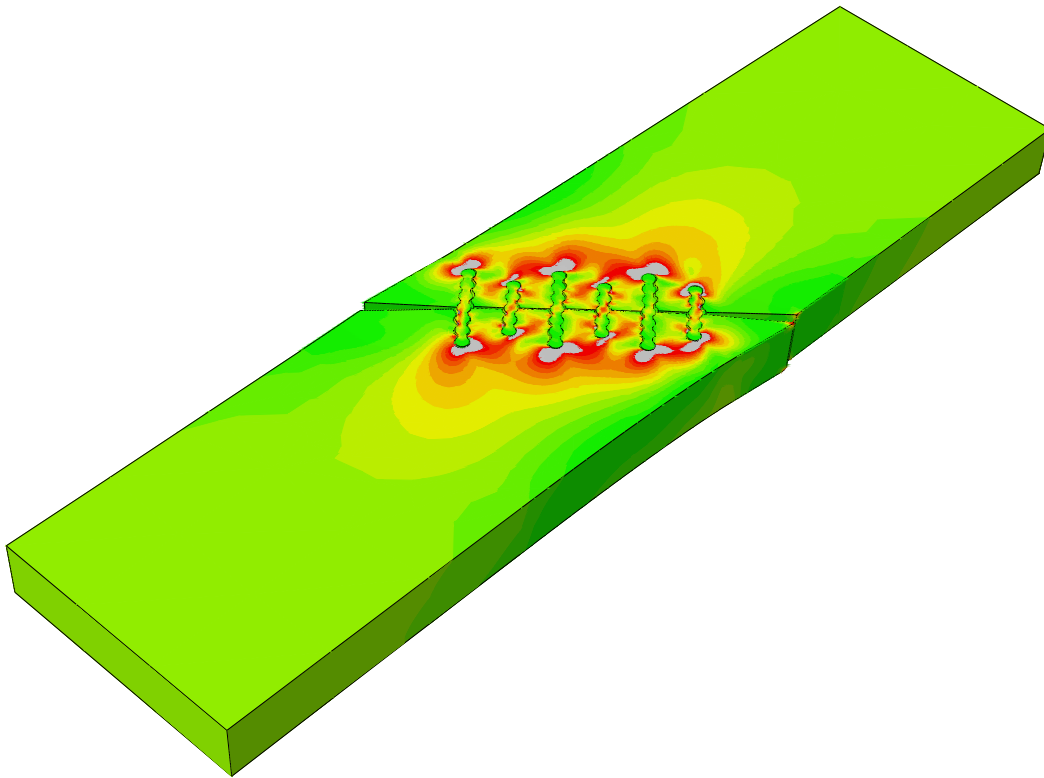


CHALMERS



Analysis of Strains in Cast Iron Joints Using FE-Simulations and Digital Image Correlation Techniques

Master of Science Thesis

ANDREAS AUTIO
KRISTOFFER ODNEGÅRD

Department of Applied Mechanics
Division of Dynamics
CHALMERS UNIVERSITY OF TECHNOLOGY
Göteborg, Sweden 2011
Master's Thesis 2011:29

Analysis of Strains in Cast Iron Joints Using FE-Simulations and Digital Image Correlation Techniques

Master's Thesis in Structural Engineering

ANDREAS AUTIO

KRISTOFFER ODNEGÅRD

Department of Applied Mechanics

Division of Dynamics

CHALMERS UNIVERSITY OF TECHNOLOGY

Göteborg, Sweden 2011

Analysis of Strains in Cast Iron Joints Using FE-Simulations and Digital Image Correlation
Techniques

ANDREAS AUTIO

KRISTOFFER ODNEGÅRD

©ANDREAS AUTIO, KRISTOFFER ODNEGÅRD, 2011

Master's Thesis 2011:29

ISSN 1652-8557

Department of Applied Mechanics

Division of Dynamics

Chalmers University of Technology

SE-412 96 Göteborg

Sweden

Telephone: + 46 (0)31-772 1000

Cover:

Maximum principal strains in a Metalock joint subjected to tensile loading.

Chalmers Reproservice

Göteborg, Sweden 2011

Analysis of Strains in Cast Iron Joints Using FE-Simulations and Digital Image Correlation Techniques

Master's Thesis in Structural Engineering

ANDREAS AUTIO

KRISTOFFER ODNEGÅRD

Department of Applied Mechanics

Division of Dynamics

Chalmers University of Technology

Abstract

The Metalock method is a mechanical joining technique most commonly employed in cracked castings of iron, aluminum and steel. It is based on inserting custom-made “keys”, which are meant to take up tensile and shear stresses, perpendicular to the crack. The marine diesel engine designer MAN Diesel & Turbo, uses the Metalock method for crack patching in large cast iron components, such as cylinder frames, in their engines. The service life of these components can thereby be significantly extended, reducing both replacement costs and environmental impact.

The purpose of this thesis was to investigate the mechanical behavior of the Metalock method and study the material properties of the components included in a Metalock joint. The material properties were determined by performing thorough material testing, and the mechanical behavior of a Metalock joint was studied by full scale testing, using a non-contact deformation measurement technique known as digital image correlation, of cast iron specimens joined together by the Metalock method. Furthermore, finite element simulations were performed, and verified by experimental results, in order to study the mechanical behavior in detail and to carry out a parametric study on some of the components included in the joint.

Results from material testing show that the material of the keys are made of an iron–nickel alloy and have a very low or even negative coefficient of thermal expansion at ordinary temperatures. Differences between initial tests and simulations indicate that the installation procedure of the joint introduce residual strains which affect the behavior of a joint subjected to mechanical loading. Experimental tests show that the distance from an edge to the first key as well as the distance between keys in a joint are important parameters which affect the load carrying capacity and the location of crack initiation. In addition, numerical simulations show that an increase of the key length yields less impact on the surrounding cast iron material, if a joint is subjected to tensile loading.

Keywords: Metalock, mechanical joining, cast iron, digital image correlation, strain field, finite element analysis.

Contents

Abstract	I
Contents	III
Preface	V
1 Introduction	1
1.1 Project Background	1
1.2 Purpose	1
1.3 Limitations	1
2 Theoretical Background	2
2.1 Cast Iron	2
2.1.1 Gray Cast Iron	2
2.1.2 Cast Iron in Marine Engine Cylinder Frames	3
2.1.3 Welding of Cast Iron	4
2.2 The Metallock Repair Method	4
2.3 Digital Image Correlation	5
2.3.1 The History of DIC	5
2.3.2 Principles	6
2.3.3 Applications	6
2.4 Material Testing	6
2.4.1 Tension Test	7
2.4.2 Hardness Test	8
2.5 Strain Hardening	9
3 Method	10
3.1 Material Testing Techniques	10
3.1.1 Analysis of Chemical Composition	10
3.1.2 Dilatometric Analysis of the Metallock keys	10
3.1.3 Tension Test	10
3.1.4 Gray Cast Iron Behavior in Compression	11
3.1.5 Hardness Test	11
3.1.6 Microscopic Analysis	12
3.2 DIC Testing	12
3.2.1 Refined Tension Test and Calibration of Material Model Parameters	14
3.2.2 Metallock Joint Testing	14
3.2.2.1 Joint with Symmetric Key Arrangement	15
3.2.2.2 Joint with 45° Inclination to the Load Direction	16
3.2.2.3 Standard Joint with Four Keyholes	16
3.3 Finite Element Modeling	16
3.3.1 Selection of Element Types	18
3.3.2 Metallock Keys	18
3.3.3 Metallock Screws	19
3.3.4 Gray Cast Iron Components	19
3.3.5 Residual Strain Simulation	19
3.3.6 Contact Modeling and Friction	20
3.3.7 Boundary Conditions	20
3.3.8 Parametric Study	21

3.3.8.1	Key Length	21
3.3.8.2	Distance Between Keyholes	21
4	Results and Discussion	22
4.1	Material Testing Results	22
4.1.1	Analysis of Chemical Composition	22
4.1.2	Dilatometric Analysis of the Metallock Keys	22
4.1.3	The First Tension Test of the Metallock Keys	24
4.1.4	Tension Test of the Gray Cast Iron	24
4.1.5	Hardness Test of the Metallock Key Material	26
4.1.6	Hardness Test of the Gray Cast Iron	27
4.1.7	Microscopic Analysis	29
4.1.7.1	Microstructure of the Metallock Key Material	29
4.1.7.2	Microstructure of the Gray Cast Iron Material	29
4.1.8	Refined Tension Test of the Metallock Keys Using DIC	30
4.2	Metallock Joint Testing and Simulation	31
4.2.1	Joint with Symmetric Key Arrangement	31
4.2.1.1	Cyclic Tension	33
4.2.1.2	Residual Strains	34
4.2.1.3	Cyclic Tension — Higher Resolution DIC Measurements	35
4.2.1.4	Cyclic Compression	37
4.2.2	Cyclic Tension Test of Standard Joint with Four Keyholes	40
4.2.3	Joint with a 45° Inclination to the Load Direction	42
4.2.3.1	Cyclic Tension	42
4.2.3.2	Cyclic Tension — Higher Resolution DIC Measurements	43
4.2.3.3	Cyclic Compression	46
4.2.4	FEM Parametric Study	46
4.2.4.1	Key Length	46
4.2.4.2	Distance Between the Keyholes	50
5	Conclusions	52
A	DIC Test Setup	54

Preface

This Master of Science thesis is an in-depth study of the mechanical behavior of a crack patching technique, known as Metallocking, primarily employed in gray cast iron structures such as marine diesel engine components.

The thesis is a result of a collaboration between Chalmers University of Technology in Göteborg, SP Technical Research Institute of Sweden in Borås, and MAN Diesel & Turbo in Copenhagen. The work was conducted at SP's facilities in Borås during the spring of 2011.

Acknowledgements

Most importantly, we would like to thank our supervisor at SP, Torsten Sjögren, Ph.D., for his supervision, the many helpful comments and suggestions, and the commitment of guiding us through this thesis. We would also like to express our gratitude to our supervisor at Chalmers University of Technology, Anders Ekberg, A/Prof., and Henrik Andersson, D.Tech., at MAN Diesel & Turbo in Copenhagen for their feedback and critical commentary, as well as for the time they have spent reading the various drafts of this thesis. Furthermore, we would like to thank Mathias Flansbjer, Ph.D., and Henrik Snygg, M.Sc., at SP for their support. We are of course also very much indebted to the rest of the helpful staff at SP for all their assistance and expertise in various areas.

Göteborg June 2011

Andreas Autio, Kristoffer Odnegård

1 Introduction

1.1 Project Background

Large cast iron components such as pumps, machine castings, gearboxes, pipe lines and engine castings might after a long time in service crack and subsequently fail. To replace such components can be both very expensive and difficult, and therefore repair is often desirable. Methods such as welding, which include heating have the drawback of introducing unwanted residual stresses and possibly changing the structure of the cast iron material creating brittle phases such as martensite. The Metalock method is a commonly used mechanical joining method for crack patching that has many advantages. No thermal stresses are introduced and since the procedure is relatively fast it minimizes downtime which can be valuable in emergency situations.

The initiative for investigating the mechanical properties of the Metalock method originates from the marine engine designer MAN Diesel & Turbo, who primarily uses the Metalock method for repair of cylinder frames in their marine diesel engines. The Metalock method has both environmental and economical benefits since it can postpone replacements of such components.

1.2 Purpose

Ever since the Metalock method was introduced, it has been accepted as an effective repair solution. However, studies of the mechanical behavior of the Metalock method are not to be found in the literature. The aim of this Master's Thesis is to:

- Investigate the mechanical properties of Metalock joining in different cases of loading, including tension, compression and shear.
- Determine the material properties of the gray cast iron and the Metalock key material by material testing, that includes tension tests, hardness tests, dilatometric tests, determination of chemical composition, and microscopic analyses.
- Simulate the material response to loading using the finite element code Abaqus [1].
- Verify finite element simulations by comparison to *in situ* digital image correlation measurement results.
- Perform a parametric study in order to investigate possible improvements of the Metalock joining technique.

1.3 Limitations

The Metalock method will be tested in tension, compression and shear. The shear test will be performed by testing a 45° rotated Metalock joint in tension and compression, which means that the joint will be subjected to a combination of shear and tension/compression. Focus will be on Metalock applications in cast iron components in general, but a particular emphasis will be on gray cast iron. Only tension tests will be performed to determine material properties, i.e. no compression tests are performed. The behavior of gray cast iron in compression will instead be achieved from previously performed compression tests of gray cast iron with similar tensile properties.

2 Theoretical Background

2.1 Cast Iron

Cast irons all have in common that they are iron–carbon alloys that have solidified in a stable (or metastable) *eutectic reaction*¹ producing graphite (or iron–carbide) and austenite. Several types of cast iron exist and all contain large amounts of carbon, typically 2 to 4 wt%, and an additional 1 to 3 wt% of silicon. Different grades of cast iron for different needs can be achieved by varying the carbon and silicon content and also by adding elements such as manganese, sulphur and phosphorous [2]. A decrease in the amount of carbon and silicon for example often yields a higher strength of the material [3].

The most common types of cast irons are white iron, gray iron, ductile iron, and malleable iron, see Table 2.1 (where *elongation in 50 mm* is a common representation of ductility expressed as the permanent extension of the gauge length after fracture with an initial gauge length of 50 mm). White iron and gray iron are named after the appearance of their fracture surfaces; because of its high content of graphite, gray iron has a characteristic gray fracture surface while white iron, which is rich in iron carbide, instead exhibits a white crystalline fracture surface [4].

Table 2.1: Common types of cast iron and typical mechanical properties [5].

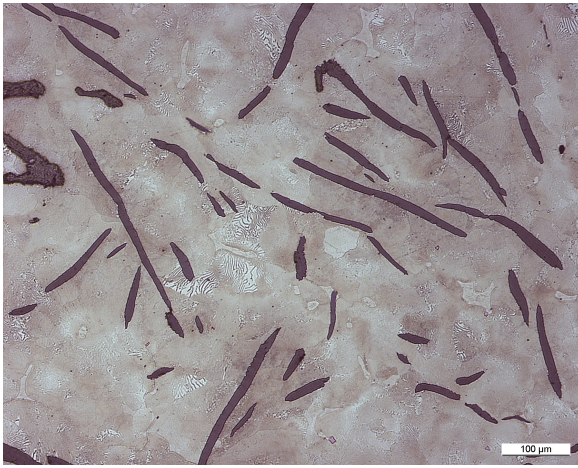
Cast Iron	Type	Ultimate tensile strength [MPa]	Yield strength [MPa]	Elongation in 50 mm [%]
Gray	Ferritic	170	140	0.4
	Pearlitic	275	240	0.4
	Martensitic	550	550	0
Ductile	Ferritic	415	275	18
	Pearlitic	550	380	6
	Tempered martensite	825	620	2
Malleable	Ferritic	365	240	18
	Pearlitic	450	310	10
	Tempered martensite	700	550	2
White	Pearlitic	275	275	0

2.1.1 Gray Cast Iron

In the solidification of gray cast iron austenite and graphite are formed by a eutectic reaction. The austenite is then further transformed in a *eutectoid reaction*² forming ferrite and cementite in an alternate lamellae structure, i.e. pearlite, see Figure 2.1b. Depending on the cooling rate, alloying and melt treatment, the matrix structure is either ferritic, pearlitic, martensitic or partly ferritic and pearlitic. Since the carbon is arranged in graphite flakes (see Figure 2.1a), gray cast iron is sometimes called *flake graphite cast iron*. The graphite flakes contribute to the material’s great damping properties, relatively

¹A process in which a liquid is transformed into two solids.

²A process in which a solid is transformed into two other solids.



(a) In 100X magnification, the graphite flakes are clearly visible.



(b) In 500X magnification, the lamellae structure of the pearlite is visible.

Figure 2.1: Micro structure of a typical gray cast iron with pearlitic structure.

good thermal conductivity and lubricating properties which makes it suitable for use in e.g. engine blocks, machine tools and other mechanical structures subjected to vibrations and/or high temperatures. The mechanical properties of this type of cast iron depend on the chemical composition, the degree of nucleation and the rate of cooling. These three parameters determine the amount of graphite and the structure of the graphite flakes in the casting, which is closely related to the tensile strength and the ductility of the material [2].

As opposed to ductile iron where the graphite is formed in a spheroid shape, the flake shape of the graphite in gray cast iron reduces the ductility of the material since the edges of the flakes create larger stress concentrations. This is why fracture in gray cast iron primarily occurs along the graphite flakes [5].

Tests have shown that tensile strength decreases as the cast section size increases. This is primarily a consequence of the difference in cooling rate experienced by the material during solidification. The slower rates of solidification in heavier castings lead to a lower number of nuclei becoming active during the eutectic reaction. This, in turn, leads to a coarse final eutectic cell size which reduces the strength properties [2].

2.1.2 Cast Iron in Marine Engine Cylinder Frames

The type of cast iron used in the cylinder frames designed by MAN Diesel & Turbo is a low alloyed gray cast iron internally called C3Cu. It has a specified carbon content of 3.2%, silicon content in the interval 1 to 2%, manganese content of 0.7%, and a copper content in the interval of 0.5 to 1.2%. Furthermore, upper limits of 0.1 to 0.2% are specified for phosphorus, sulphur and tin. The amount of silicon and copper are balanced depending on the cast section size. Heavier structures are for example composed of the higher levels of copper and the lower levels of silicon in order to achieve a pearlitic structure [6].

The tensile strength of the material is specified according to Table 2.2, where “separate casting” refers to a specimen cast separately in a smaller section, “cast on” refers to a smaller exerted part which is removed from the cast component after solidification and “casting” refers to a specimen extracted from a large cast section.

Table 2.2: Tensile strength specifications for gray cast iron of type C3Cu [6].

Sample type	Dimension [mm]	Tensile strength [MPa]
Separate casting	-	250
Cast on	-	150
Casting	< 80	150
Casting	≥ 80	140

2.1.3 Welding of Cast Iron

There are several reasons for avoiding heat treatment of cast iron. Because of their porous metallurgical structure, cast irons tend to absorb oils and other fluids which affect the weldability. Prior to welding these fluids need to be removed in a process that also involves heating. This operation is impossible in most situations where the component geometry is complex [7].

In addition, the high carbon content significantly affects the weldability of the material. During welding, when the material is heated above the eutectoid temperature (727 °C), the carbon dissolved in ferrite and cementite can transform back to austenite in a reverse eutectoid reaction [4]. When the austenite cools rapidly its fcc³ atomic structure is transformed to a bct⁴ structure instead of a bcc⁵ structure. This atomic structure, called *martensite*, has a rectangular shape and does not have as many slip systems as a bcc structure and is therefore extremely hard and brittle. Furthermore, during this transformation the volume of the material might increase by as much as 4%, causing internal stresses and possibly cracks [5].

2.2 The Metalock Repair Method

The Metalock method was developed in 1947 in the United Kingdom by the company Metalock Engineering Ltd. It is a world-wide acknowledged mechanical equipment repair technique for cracked, broken and damaged castings in iron, aluminum and steel with a variety of applications in e.g. Mechanical and Civil Engineering.

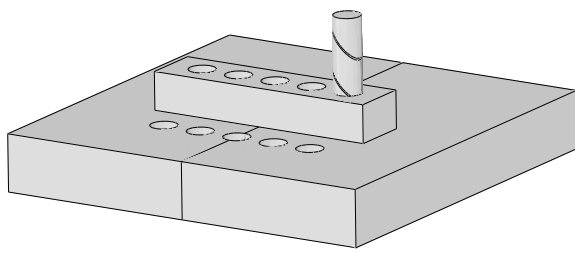
The repair is based on inserting individually designed Metalock keys and Metalock screws manufactured from a special iron–nickel alloy into the crack. Using a drill jig, holes are drilled close to each other in rows perpendicular to the crack. The intermediate partitions are mechanically removed using a pneumatic chisel. The resulting cuts are filled with several layers of Metalock keys which are meant to take up both tensile and compressive stresses. In order to seal the crack, new holes are drilled along the crack between the keys and at both ends of each key, where Metalock screws are inserted. Finally, the entire installation is caulked to ensure stability and pressure tightness. In some cases the joint is machined in order to smoothen the surface and eliminate stress concentrations. Figure 2.2 shows the main steps of the procedure.

The advantages of Metalock repairing compared to other types of repairing techniques are that the work can be done *in situ* in a short time and that no heating is involved i.e. no heat-affected zone is introduced. The strength of the Metalock keys provides the repaired construction with a high percentage of the original strength [8].

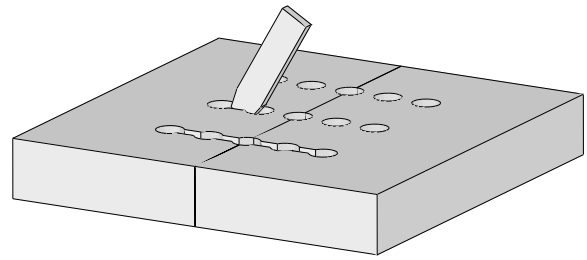
³Face-centered cubic

⁴Body-centered tetragonal

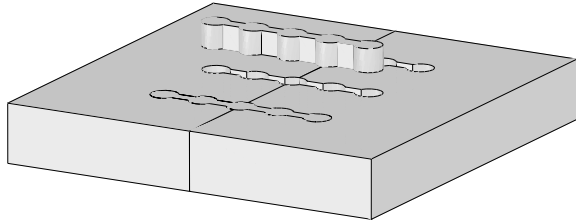
⁵Body-centered cubic



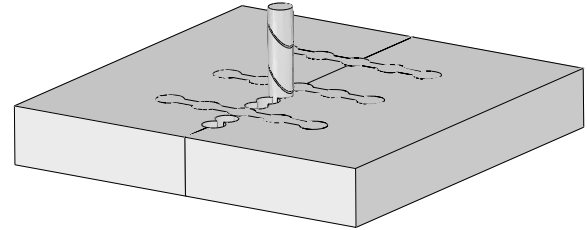
(a) Holes are drilled in a certain pattern perpendicular to the crack in the broken component.



(b) The walls between the holes are removed to fit the Metallock keys.



(c) The Metallock keys are inserted.



(d) New holes are drilled along the crack and at the ends of the keys where the Metallock screws are inserted.

Figure 2.2: The Metallock method, step by step.

2.3 Digital Image Correlation

Digital Image Correlation (DIC) is a non-contact deformation measurement technique, based on gray value digital images, that can determine the strains and the displacements of a loaded object in three dimensions. Due to the rapid development of computational power and optical sensors in recent years the application for DIC has broadened and it has proven to be a flexible and powerful tool for static as well as dynamic deformation analysis [9]. The description of DIC in the following section is a summary of the detailed description that can be found in Sutton, Orteu & Schreier.

2.3.1 The History of DIC

Early works in the field of image correlation was done by Gilbert Hobrough in the 1950s. He used analog photographs of objects from different views in attempts to register features. By 1961 Hobrough had developed the method and built an instrument to “correlate high-resolution reconnaissance photography with high precision survey photography in order to enable more precise measurement of changeable ground conditions”. This can be seen as the first utilization of the image correlation principle to extract positional information from an image matching process.

In the 1960s and 1970s digitized images became available which led researchers in the fields of robotics and artificial intelligence to further develop the DIC principle for applications in character recognition, microscopy and medicine. Engineering applications for shape and deformation measurements were however at this time rarely used.

In the 1980s the first computer-based image acquisition and deformation measurements in material systems were investigated. A technique to compare various small regions (known as *subsets* or *facets*) throughout the digital images before and after deformation was developed using digital image analysis in order to locate the positions of each of these subsets. As a part of the approach, researchers used fundamental continuum mechanics concepts describing the deformations of small areas as part of the matching process.

In 1985 a series of experiments were performed that showed that the method could be applied for quantifying both rotations and displacements in solids, and numerical algorithms using gradient search methods were developed in order to improve the speed of the analysis process.

2.3.2 Principles

The general idea of DIC is to distinguish the difference in the surface pattern in a series of images of an object by using mathematical algorithms. This operation has certain difficulties. The major issue is known as the *correspondence problem*, which could be described as the difficulty in finding a unique correspondence between series of images of an object in motion. In images built up by millions of gray scale pixels it is often impossible to uniquely determine the location of one single pixel from one image to the next. The exact same gray scale value can be apparent in thousands of pixels throughout the image. In order to resolve this issue one needs to consider a larger area around the point of interest so that a unique correspondence can be found. This is even more of an issue if the measured object also undergoes deformation in the series of images. For a blank and textureless object it is not possible to determine movements of single points within the boundaries because no features are present, and if the object undergoes deformation it is even impossible to establish motion vectors along the boundaries of the object.

In order to overcome the correspondence problem it is necessary to provide the surface with certain properties that help to determine the position of subregions. Repeating patterns are not preferable because they can lead to misregistration problems. Instead a stochastic speckle pattern is used that deforms with the surface. This speckle pattern can either occur naturally in the material or be applied by for example spraying the surface with black and white paint.

By using two cameras and recording images from two views simultaneously, it is possible to establish three-dimensional measurements of e.g. deformation in objects. Knowing the imaging parameter and the orientation of the cameras with respect to each other, the position of each object point in three dimensions can be calculated by applying correlation algorithms.

2.3.3 Applications

Today there is a large and growing number of applications for DIC. Research for applications in fracture mechanics, fluid dynamics and micro-scale deformation measurements using scanning electron microscopes began in the 1980s and continues to this day. The method can be successfully used for identification of material parameters far into the range of plastic deformation. It allows the determination of the location and magnitude of maximum strain, which are important parameters in material testing. The method is applicable for a large number of materials e.g. steel, aluminum, concrete, wood, rock and polymers. Since the method in theory delivers exact information of local and global strain distribution and of crack growth it is very suitable for applications in fracture mechanics.

2.4 Material Testing

Material testing is necessary in order to determine material strength and other properties of interest. In this section two of the most common tests are described.

2.4.1 Tension Test

A common tension test results in *nominal* stress–strain data, i.e. force per unit undeformed area versus length change per unit undeformed length. Because of the fact that the specimen is experiencing necking during the tension test, the maximum *nominal stress*⁶ measured will be lower than the material’s *ultimate strength*⁷. This also means that the maximum strain measured is lower than the material’s maximum strain, since the measured strain is merely a mean value over the gauge length of the extensometer [10]. Further, this leads to different results in tension and compression even for materials that theoretically have the same tensile and compressive properties, since the necking phenomenon does not occur in a compression test. A model describing the plastic behavior of a material should be able to account for differences in compressive and tensile behavior, independent of possible changes in the geometry of the object. This is done by introducing the so called *true stress* and *true strain* that account for the change in cross-sectional area during deformation [11].

The true strain or *logarithmic strain* is defined by considering an incremental length in the limit as $\Delta\ell \rightarrow d\ell \rightarrow 0$; i.e.,

$$d\varepsilon = \frac{d\ell}{\ell} \quad (2.1)$$

which leads to

$$\varepsilon = \int_{\ell_0}^{\ell} \frac{d\ell}{\ell} = \ln\left(\frac{\ell}{\ell_0}\right) \quad (2.2)$$

where ℓ is the current length and ℓ_0 is the original length. In contrast the nominal strain can be expressed as

$$\varepsilon_{\text{nom}} = \frac{\ell - \ell_0}{\ell_0} = \frac{\ell}{\ell_0} - 1 \quad (2.3)$$

This gives an expression for the true strain, ε , in terms of the nominal strain as

$$\varepsilon = \ln(1 + \varepsilon_{\text{nom}}) \quad (2.4)$$

Further, true stress is defined as

$$\sigma = \frac{F}{A_i} \quad (2.5)$$

where F is the force in the material and A_i is the current cross-sectional area. By considering the incompressible nature of the plastic deformation and assuming that the elasticity is also incompressible, the relation between true stress and nominal stress can be expressed from the relationship

$$\ell_0 A_0 = \ell A_i \quad (2.6)$$

where A_0 is the nominal cross-sectional area. This can be rewritten in order to formulate an expression for the current area, A_i , as

$$A_i = A_0 \frac{\ell_0}{\ell} \quad (2.7)$$

Inserting this into Eq. 2.5 gives the true stress, σ , as

⁶The average stress over the initial cross-sectional area of a specimen.

⁷The maximum stress that a material, loaded in tension, can withstand before necking occurs.

$$\sigma = \frac{F}{A_0} \frac{\ell}{\ell_0} = \sigma_{\text{nom}} \left(\frac{\ell}{\ell_0} \right) \quad (2.8)$$

Finally, using Eq. 2.3 the true stress can be expressed in terms of the nominal stress and nominal strain as

$$\sigma = \sigma_{\text{nom}}(1 + \varepsilon_{\text{nom}}) \quad (2.9)$$

Using Eq. 2.4 and Eq. 2.9 the nominal stress and strain can be converted into the true stress and strain [11]. However, when the material is approaching its failure strain and the cross sectional area and length of the specimen starts to change substantially (i.e. heavy necking) the true stress–strain relation can no longer be described using Eq. 2.4 and Eq. 2.9. In order to properly describe the true stress–strain relation after this point, the varying minimum cross-sectional area needs to be measured during the tension test [10]. The true stress is then calculated using Eq. 2.5 and the true strain is calculated as

$$\varepsilon = \ln \frac{A_i}{A_0} \quad (2.10)$$

To measure the shrinking cross-sectional area of the specimen during testing can be difficult, why instead an approximation for the true stress–strain relation beyond the yield limit can be expressed by the so called Hollomon power relation defined as

$$\sigma = K \varepsilon_{\text{pl}}^n \quad (2.11)$$

where K is a strength coefficient, n is a strain hardening exponent and ε_{pl} is the true plastic strain. In order to obtain the parameters K and n the nominal stress–strain relation is recalculated to represent the true stress–strain relation using Eq. 2.4 and Eq. 2.9, and the region from initial yielding to the ultimate tensile strength is numerically curve fitted to the power relationship in Eq. 2.11.

Various quantities can be extracted from the stress–strain relationship obtained in a tension test. Initially, the stress–strain relation may be linear, describing the elastic stiffness of the material. The *Elastic modulus* or *Young's modulus* can be obtained from two points on the linear part of the nominal stress–strain curve as

$$E = \frac{\sigma_2 - \sigma_1}{\varepsilon_2 - \varepsilon_1} \quad (2.12)$$

Some materials do not have a pronounced linear region and in these cases a *tangent modulus*, E_t , may be employed, which is the derivative of the stress–strain curve at the origin or at some chosen stress level, and it is expressed as

$$E_t = \frac{d\sigma}{d\varepsilon} \quad (2.13)$$

Another important parameter is the material's yield limit, which can be defined using the so called *offset method*. A straight line is drawn parallel to the elastic region of the nominal stress–strain curve but offset by a strain of 0.002, i.e. 0.2%. The intersection of this line with the nominal stress–strain curve is defined as the *offset yield strength*, σ_o [10].

2.4.2 Hardness Test

For engineering purposes, the hardness of a material is generally a measure of the resistance to *indentation*. Usually, hardness is measured by pressing a ball or a point with a specific

weight to the surface of the material and then measuring the size of the indent that it leaves due to plastic deformation. A measure of the size or depth of the indentation is then used to define the hardness of the material [10].

The Brinell and Vickers hardness tests are among the most commonly used hardness tests for engineering purposes. They differ in the shape of the indenter, in the Brinell test a steel ball is used whereas in the Vickers test a diamond point in the shape of a pyramid is used. The Brinell hardness number, abbreviated HB , is calculated by dividing the applied force P by the area of the curved surface of the indentation as

$$HB = \frac{2P}{\pi D(D - \sqrt{D^2 - d^2})} \quad [\text{kg/mm}^2] \quad (2.14)$$

where D is the diameter of the ball and d is the diameter of the indentation [12]. The Vickers hardness number, HV , is calculated by dividing the applied force by the pyramidal depression as

$$HV = \frac{2P}{d^2} \sin \frac{\alpha}{2} \quad [\text{kg/mm}^2] \quad (2.15)$$

where d is the diagonal of the indentation and $\alpha = 136^\circ$ is the angle between the phases of the pyramid [12]. For carbon alloyed steels, the hardness is approximately linearly related to the ultimate tensile strength, and hence hardness measurements can be used to make predictions of the strength properties of the material [10].

2.5 Strain Hardening

Strain hardening, sometimes called *cold-working*, is a process that is used to strengthen metals or alloys by decreasing the size of the material in one or two dimensions which causes an increase in the other dimensions. The grains in the principal direction of the cold-work are severely elongated which causes a reorientation of the grains in a preferred direction. The effect of strain hardening is primarily an increase in the tensile properties of the material. In addition some other physical properties are affected to some extent. The density is generally decreased by a few tenths of a percent, the electrical conductivity is usually decreased while the thermal coefficient of expansion is increased. The chemical reactivity is increased which leads to a higher sensitivity for corrosion and for some alloys a risk for stress-corrosion cracking is introduced [12].

The basic equation describing the increase of strength due to strain hardening is given as

$$\sigma_o = \sigma_i + \alpha G b \rho^{1/2} \quad (2.16)$$

where σ_o is the yield strength after strain hardening, σ_i is the initial yield strength, α is a unitless correction factor specific to the material, G is the shear modulus in [Pa], b is the *lattice constant* in [m], and ρ_\perp is the dislocation density in [m/m^3] [12].

3 Method

3.1 Material Testing Techniques

It is necessary to determine the material properties of the Metallock keys and the gray cast iron components in order to get a deeper understanding of the mechanical behavior of the Metallock method and to be able to obtain a sophisticated finite element model. One way to define plasticity properties in Abaqus is to approximate the smooth stress–strain behavior with a series of straight lines joining given data points, obtained from tension tests [11]. Further, hardness tests are performed, and the materials are subjected to microscopic analysis to get a better general knowledge of the materials. The Metallock key material is additionally analyzed with respect to the chemical composition, and the coefficient of thermal expansion is determined.

3.1.1 Analysis of Chemical Composition

Since the material that the Metallock keys are composed of was not known, an analysis of the chemical composition was needed. The carbon and sulfur content of the Metallock keys was determined by infra-red detection of CO₂ and SO₂ created from oxygen combustion of the material in a high-frequency inductive furnace.

The amount of other elements was determined using X-ray fluorescence. This method is a semi-quantitative analysis of the *surface layer* that gives an estimation of the content of specific elements. It is primarily applicable for elements in the periodic table with atomic numbers greater than nine [4].

The results from the analyze can be found in Section 4.1.1.

3.1.2 Dilatometric Analysis of the Metallock keys

A dilatometer of type Netzsch DIL402, was used to determine the coefficient of thermal expansion for the Metallock key material. Using a push rod, the expansion (or contraction) during heating is measured for a material. The dilatometer uses a Linear Differential Variable Transformer (LDVT) to convert the push rod displacement to voltage, which is then recorded and converted to a displacement signal. By controlling and recording the temperature of a sample at the free end of the push rod, the *linear* coefficient of thermal expansion can be calculated as

$$\alpha = \frac{1}{L_0} \frac{dL}{dT} \quad (3.1)$$

where L_0 is the initial length of the test specimen and dL/dT is the rate of change in length per unit change in temperature [4].

Two samples with the dimensions $25 \times 4 \times 6 \text{ mm}^3$ were cut out from a Metallock key component and the coefficient of thermal expansion was determined with a heating rate of 4 K/min and 10 K/min respectively in the temperature range $T = 30^\circ\text{C}$ to $T = 450^\circ\text{C}$. The results are presented in Section 4.1.2.

3.1.3 Tension Test

Both the Metallock keys and the gray cast iron components were subjected to tension tests. For the keys, test specimens with square cross sections were created by machining Metallock key components. Test specimens with a round cross section were created by cutting pieces from the gray cast iron components used in the Metallock joint testing. Details regarding

the test specimens are listed in Table 3.1. All tests were performed using two specimens, in a test machine with a load cell of 100 kN, and with position as the control channel. The strain rate was 1 mm/min. The Metallock key material was tested in two turns, with and without the aid of DIC.

The results from the tension test are presented in Section 4.1.3

Table 3.1: Test specimen details.

Test	Cross section	Width/ diameter [mm]	Cross sectional area [mm ²]	Specimen length [mm]
Metallock Keys				
Tension test	Square	4	16	40
DIC aided tension test	Square	4	16	40
Gray Cast Iron				
Tension test	Round	10	78.5	72

3.1.4 Gray Cast Iron Behavior in Compression

No compression tests were performed on the gray cast iron material, the stress–strain curve in compression was instead obtained from previous tests, performed by Sjögren [13], of a similar gray cast iron material. The stress–strain relation, furthermore used as material input in Abaqus, is shown in Figure 3.1 and it can be noted that the relation is close to linear.

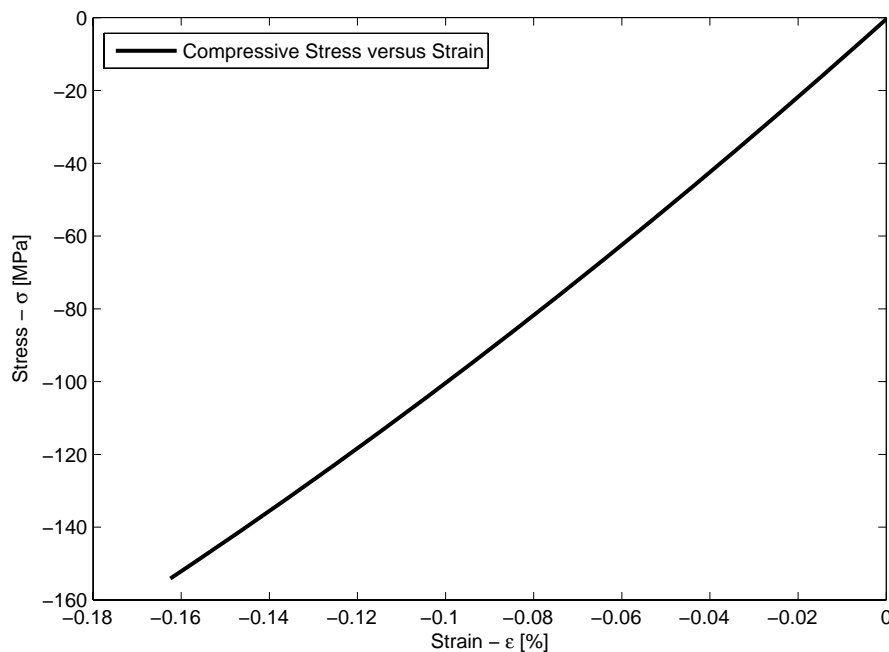


Figure 3.1: Gray cast iron stress–strain behavior in compression.

3.1.5 Hardness Test

In the installation of the Metallock keys in a Metallock joint, the keys are hammered into place. Hardness tests were performed on both used and unused Metallock keys since the

hammering treatment may cause the material to undergo plastic deformation and therefore change the hardness properties of the material. Furthermore, the Metalock keys may also have been subjected to cold working in the manufacturing process that may affect the hardness properties. In addition, a hardness test was performed on one of the specimens from the material tension tests in order to investigate the effect of pure tension on the hardness distribution.

The experimental conditions for the hardness tests are described in Table 3.2 and the results are presented in Section 4.1.5 and Section 4.1.6. For hardness measurements on the gray cast iron material, the Brinell method was used. The reason for this is that the microstructural composition of gray cast iron, consisting of soft graphite flakes and pearlite/ferrite in an alternate structure, makes points unsuitable since the exact location of the indent may or may not coincide with a graphite flake. For the Brinell tests, a ball diameter of $d = 10$ mm was used.

Table 3.2: Experimental conditions for the hardness tests.

Test	Load [kg]	Tested area [mm ²]	Indent distance [mm]	No. of indents
Metalock Keys				
(Vickers)				
Unused	2	30.0×3.5	0.5	488
Used	2	24.5×2.5	0.5	298
Tension tested	2	29.5×3.0	0.5	383
Gray Cast Iron				
(Brinell)				
Specimen	3000	-	25	6

3.1.6 Microscopic Analysis

The microscopic analysis was performed (in $100\times$ magnification) with a microscope that uses image analysis to categorize the gray cast iron phases. 72 gray scale images showing an area of $\sim 278 \mu\text{m}^2$ each, taken in $100\times$ magnification were combined in a mosaic (showing a total area of $\sim 20 \text{ mm}^2$) and a software coupled to the microscope was then used to determine the amount of graphite, pearlite, and ferrite in the specimen. The results are presented in Section 4.1.7.1.

3.2 DIC Testing

A system of DIC hardware and software called Aramis was used for the calculation and analysis of strain fields in the experimental testing of the Metalock keys and Metalock joints. This system uses the DIC principle, as described in Section 2.3, to recognize the surface structure of the measuring object in three dimensions and allocate coordinates to the digital camera image pixels. In order for the software to be able to recognize a speckle pattern, the measuring surface is covered with white spray paint and then sprayed with black paint dots in a stochastic pattern. An example of such a random speckle pattern is shown in Figure 3.2.

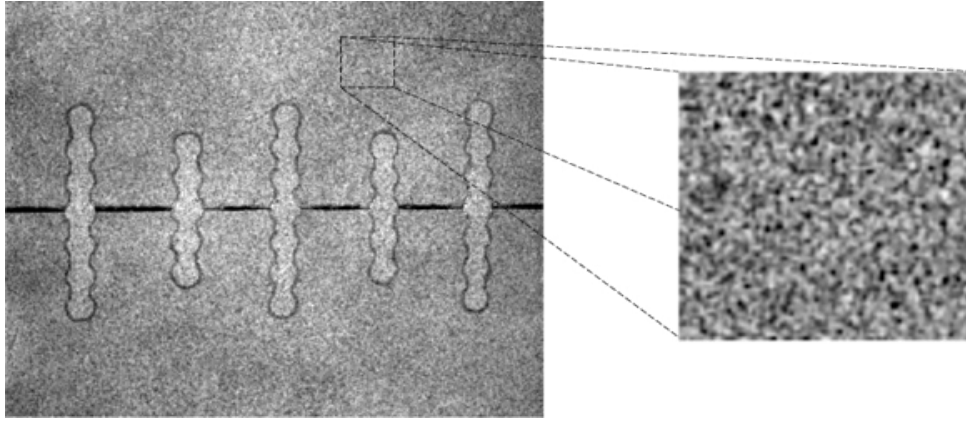


Figure 3.2: Speckle pattern that helps the Aramis system to recognize surface characteristics of the test object.

The Aramis system features a possibility for a graphical representation of the measurement results with a user defined color scale. This makes it easy to visually compare the DIC measurement results to finite element calculations for a rough verification of the FE simulations.

The employed Aramis system consisted of the following hardware and software components:

- Sensor with two digital cameras
- Stand for steady hold of the sensor
- Controller for power supply and to control image recording
- PC system
- Aramis v6.1 and GOM Linux 10

Prior to measuring, the Aramis equipment needs to be calibrated for the specific purpose, i.e. the size of the test object and the level of desired detail in the measurement. This is done by adjusting the cameras so that the angle between the cameras and the distance to the object correspond to optimal values — according to a configuration table provided by the manufacturer — for capturing the object in the measuring volume. The calibration is done using calibration objects of varying sizes depending on the application, and the purpose is to obtain dimensional consistency of the measuring system. The calibration objects are panels that are equipped with reference points that help the system establish a three dimensional coordinate system [14].

After the Aramis test is performed the recorded data needs to be post-processed. The post-processing consists of choosing the areas of the test to be analyzed, and choosing the size and overlap of the facets. The areas of interest are chosen by masking the parts of the images that can cause errors in the strain calculations, such as voids between different parts of the test specimen. These voids will cause errors in the strain evaluations in Aramis and therefore need to be masked prior to the strain calculation. The choice of size and overlap of the facets affect the accuracy of the strain analysis. A larger facet size gives a more accurate strain evaluation since the strain calculations are based on larger number of pixels. Large facets, however, have the drawback of decreasing the resolution in the analyzed area since each facet acts as a pixel in the masked image. A smaller facet size gives a higher resolution but gives a less accurate strain evaluation. The facet overlap affects the density of the measuring points, and a large density results in a more accurate

strain evaluation [14]. The default settings in Aramis for the facet size is 15×15 pixels with a facet step of 13 pixels (corresponding to an overlap of 2 pixels).

3.2.1 Refined Tension Test and Calibration of Material Model Parameters

Since it was noticed from the hardness tests and the microscopic analysis, see Section 4.1.5 and Section 4.1.7.1, that the Metallock keys had different hardness and hence different strength properties in different sections throughout the specimen length, the material properties achieved from the first tension test were not considered to be reliable. To further investigate the material properties of the Metallock keys, a second tension test was performed using the DIC principle and the Aramis system. This allows for so-called virtual extensometers to be placed on the registered images of the test specimen after a tension test has been carried out, and hence a more detailed investigation of the stress–strain relation in different sections of the tested specimen is possible.

Virtual extensometers were placed on the parts unaffected by strain hardening in order to measure the stress–strain relation in these areas. From the obtained stress–strain relation Young’s modulus, ultimate tensile strength, and yield strength were calculated and the measurement data in the interval $[\sigma_o, \sigma_u]$ from the two tension tests were first recalculated to represent the true stress and true strain values and further numerically curve fitted against the Hollomon relation, using Matlab, to obtain the strength coefficient K and the strain hardening exponent n as described in Section 2.4.1. The mean values of K and n were then used to describe the true stress–true strain relation of the material.

In contrast to the parts unaffected by cold working, no distinct strains could be measured by the Aramis system in the cold worked parts of the material, why other techniques to achieve an estimate of the material parameters in the hardened sections were necessary. To this end, material parameters in a finite element model of a tension test specimen were calibrated toward test data.

Calibration of model parameters is in general an optimization problem, and the solution generally involves numerical least squares curve fitting. In the case of the Metallock keys, a manual iteration method was used. As experimental data employed to calibrate the model parameters, the measured strain versus section length in a middle section of the test specimen was used. Further, the test specimen was modeled using Abaqus and partitioned so that the relative size of the hardened parts and non-hardened parts matched the hardness distribution as seen in Section 4.1.5. The non-hardened material properties achieved from the Aramis measurements were then used to model the non-hardened parts whereas the hardened parts were modeled using the same material data but with a higher yield strength found by simulation iterations. In order to compare the Aramis measurement to the Abaqus simulation, and in that way calibrate the increase of the yield strength, the measured and simulated strain at points along the middle section of the test specimen were plotted respectively. When the elongation of the test specimen becomes large, severe necking occurs in the weakest point. This was simulated by weakening the material in the middle part of the specimen by using material data corresponding to the stress level in the non-hardened stress–strain relation multiplied by 0.8.

All results from the refined tension tests of the Metallock keys can be found in Section 4.1.8.

3.2.2 Metallock Joint Testing

A number of Metallock joint test specimens, all consisting of two gray cast iron blocks (cast as separate castings) with a width of 140 mm, thickness of 30 mm and length varying from 270 mm to 350 mm, joined together using the Metallock method were tested in tension and

compression. Primarily two types of specimens were tested. The first type was specimens with a symmetric arrangement of the keys (7-5-7-5-7 heads) without any Metalock screws, and the second type was specimens with joints inclined 45° to the load direction, with six Metalock keys (7-5-7-5-7-5 heads) that had Metalock screws drilled along the joint. In addition a standard type of joint (with a 7-5-7-5 key arrangement) with a distance between the keys varying from 27 mm to 31 mm, and screws along the joint was tested.

Both main specimen types were subjected to two types of loading: cyclic tension and cyclic compression (followed by tension to failure) see Table 3.3. The tests were recorded, using the Aramis system, with a measurement area covering the entire joint to be able to determine the strain distribution on a synoptical level. In addition, to be able to better observe local effects in the areas around the Metalock keys, a smaller measurement area (which means a higher resolution) focused around two of the middle keys was used on both main specimen types tested in cyclic tension.

All test specimens were made of gray cast iron of type C3Cu as specified in Section 2.1.2. The specimens were produced with Metalock keys (see Figure 3.3) of different lengths and some of the test specimens consisted of Metalock screws with a diameter of 6 mm inserted along the crack. Prior to testing the surface of the specimens were milled a few tenths of a millimeter to remove irregularities in the area of the joint. This area was then sprayed with white and black paint creating a speckle pattern.

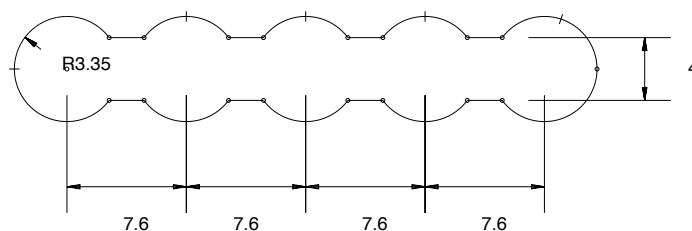


Figure 3.3: Metallock key dimensions [mm].

Table 3.3: The two different loading schemes used in the tests of the Metallock joints.

Type of loading	Loading scheme [kN]
Cyclic tension	0–50–0–100–0–150–0–Failure (tension)
Cyclic compression	0–(-50)–0–(-100)–0–Failure (tension)

In Table A.1 and Table A.2 in Appendix A a detailed overview of the parameters used in the test setups and the post-processing of the Aramis strain evaluations is shown. The calibration panel size corresponds to the maximum area that the cameras are focusing on in the analysis. The larger calibration panel with an area of $210 \times 210 \text{ mm}^2$ made the whole joint visible in the analysis, while the smaller calibration panel with an area of $65 \times 52 \text{ mm}^2$ allowed for a more detailed view of only a few of the Metallock keys.

3.2.2.1 Joint with Symmetric Key Arrangement

Three specimens (test numbers 1, 2, and 3 in Appendix A) without Metalock screws, and with symmetric key arrangements consisting of five Metalock keyholes with a center-to-center distance of 25 mm, see Figure 3.4, were tested in a test machine with a load cell of 1 MN and a grip pressure of 150 bar. The tests were performed in both cyclic tension and cyclic compression with the larger measurement area, and additionally the last test

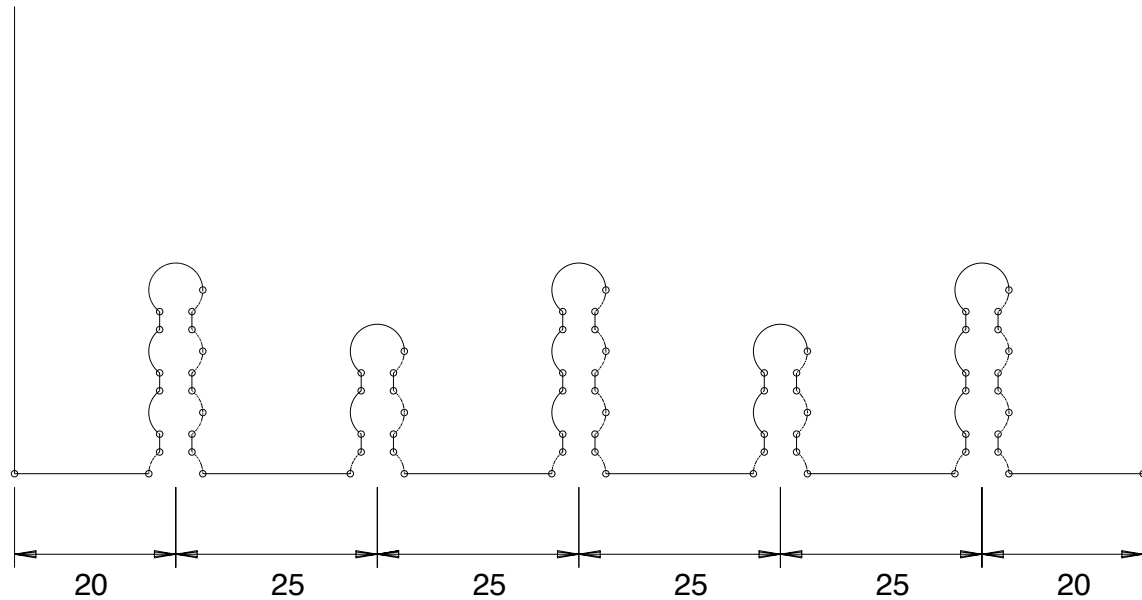


Figure 3.4: Geometry of the symmetric joint [mm].

specimen was tested in cyclic tension with the smaller measurement area. Further, one test specimen (test number 8 in Appendix A), with the same arrangement as the other three except from that it also had Metallock screws along the joint, was tested in cyclic tension in a test machine with a load cell of 500 kN and a grip pressure of 150 bar. All the tests were displacement controlled with a displacement rate of $dL/dt = 0.5$ mm/min. The results are presented in Section 4.2.1,

3.2.2.2 Joint with 45° Inclination to the Load Direction

Three specimens (test numbers 4, 6, and 7 in Appendix A) with joints inclined 45° to the load direction were tested. The joints consisted of six Metallock keys arranged 7-5-7-5-7-5 with a center-to-center distance of 21 mm and Metallock screws along the joint, see Figure 3.5. The tests were performed in a test machine with a load cell of 500 kN, a grip pressure of 150 bar and a displacement control rate of $dL/dt = 0.5$ mm/min. Three different setups were used; first cyclic tension with a large measurement volume, second cyclic compression with a large measurement volume, and third cyclic tension with a smaller measurement volume. The results are presented in Section 4.2.3.

3.2.2.3 Standard Joint with Four Keyholes

A joint with a standard key arrangement (test number 5 in Appendix A), with four keyholes and Metallock screws along the joint was tested in cyclic tension in a test machine with a load cell of 500 kN and with a grip pressure of 100 bar. The dimensions of the joint are presented in Figure 3.6, where also the Metallock screw-holes are shown. Once again, the test was displacement controlled with a displacement rate of $dL/dt = 0.5$ mm/min. The results are presented in Section 4.2.3.1.

3.3 Finite Element Modeling

The tool used for finite element simulations is Abaqus/CAE 6.10-1 with the finite element solver Abaqus/Standard. This section describes the FE-simulation procedure with respect to material modeling, choice of element types and approach regarding contact modeling in

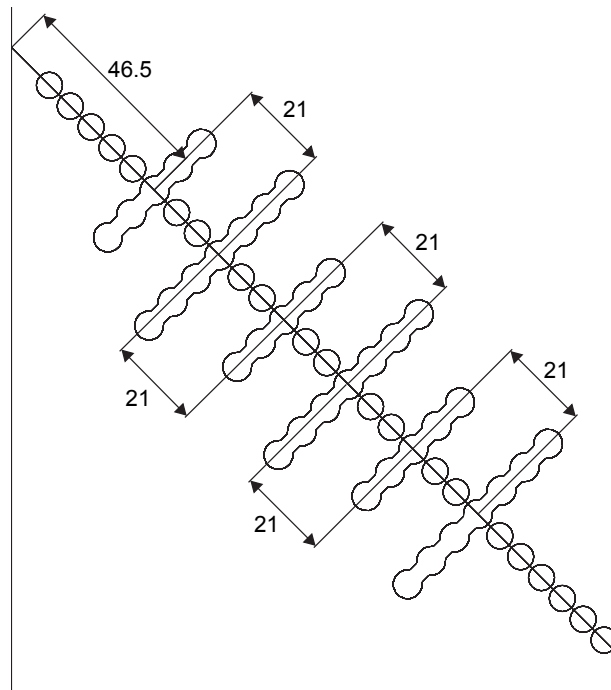


Figure 3.5: Geometry of the inclined joint [mm].

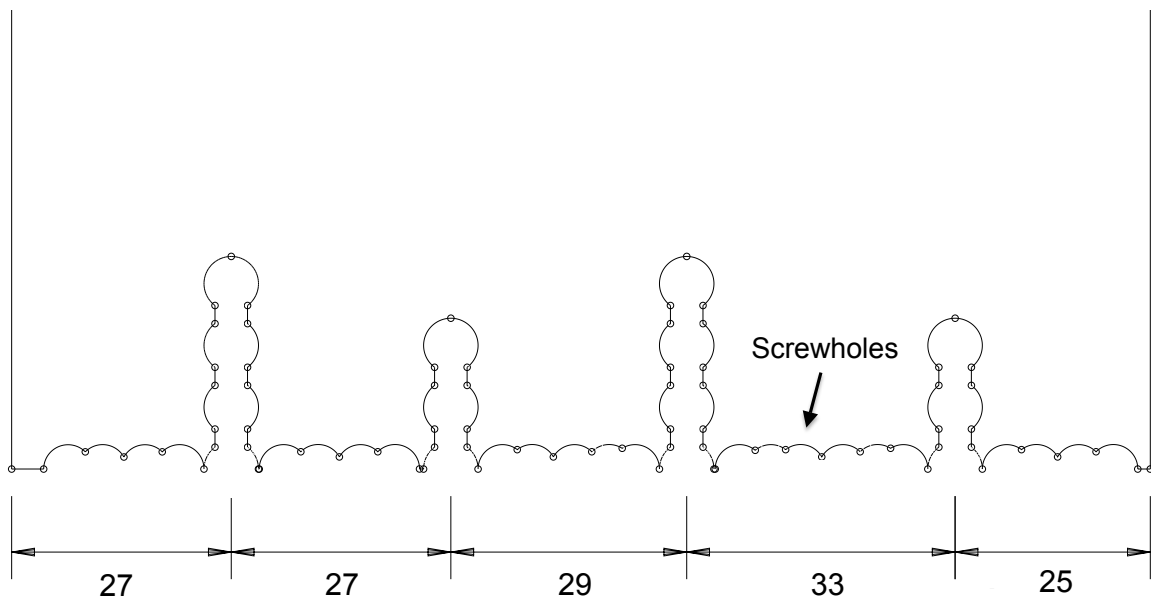


Figure 3.6: Geometry of the standard joint [mm].

Abaqus. In the test specimens that are symmetric with respect to the Metallock joint, this symmetry condition was used to reduce the size, and thereby also the number of elements, of the models.

3.3.1 Selection of Element Types

The primary type of elements chosen in the modeling of the Metallock keys, Metallock screws and cast iron components are three dimensional continuum 8-node linear brick elements called *C3D8*. These are fully integrated ($2 \times 2 \times 2$ integration points) elements of the first order and they are well suited for stress calculations. Because of the complexity in the geometry in certain regions, the brick elements are supplemented by three dimensional continuum 6-node linear triangular prism elements called *C3D6*. Since these linear prism elements tend to be overly stiff for applications in structural calculations [1], they are used only selectively for completeness of the mesh geometry.

3.3.2 Metallock Keys

When modeling a material with an elasto-plastic behavior in Abaqus the elastic part is defined by Young's modulus and Poisson's ratio, while the plastic part consists of true stress-strain relationships extracted from testing. Abaqus uses linear interpolation of stress-strain data. Therefore it is important to have a sufficient number of data points to obtain a smooth curve [11].

Since measurement data always contains a certain amount of noise, the material data obtained in the tension tests cannot be used in Abaqus without smoothing the curves. In the modeling of the Metallock keys, the nominal results from the tension tests were converted, as described in Section 2.4.1, to represent the true stress-strain relation and further curve fitted to the Hollomon relation, see Eq. 2.11. In order to obtain a smooth curve of data points with equally spaced values of strain, a strain vector consisting of 200 equally spaced values between zero and the maximum true plastic strain was created, using Matlab. The corresponding values of stress at every element of the vector were then calculated using the Hollomon relation and the resulting stress and strain vectors were used as input data to the Abaqus plasticity model.

In order to reflect the fact that the Metallock keys seem to have different properties in different parts, the Metallock keys in the model were partitioned, as shown in Figure 3.7, and two different section assignments with different material properties were used for the heads and the necks respectively. The heads were assigned with the material properties, obtained from the DIC aided tension tests, of the parts of the iron-nickel alloy test specimens unaffected by strain hardening, whereas for the necks, the strain hardened iron-nickel alloy material properties obtained by calibration of model parameters, as described in Section 3.2.1, were used.

The keys in a Metallock joint are inserted in several layers and the number of layers depend on the thickness of the mended component. The total thickness of the gray cast iron block is 30 mm and the holes for the keys are in this case 25 mm. This makes room for four keys, each with a thickness of 6.25 mm, in each hole.

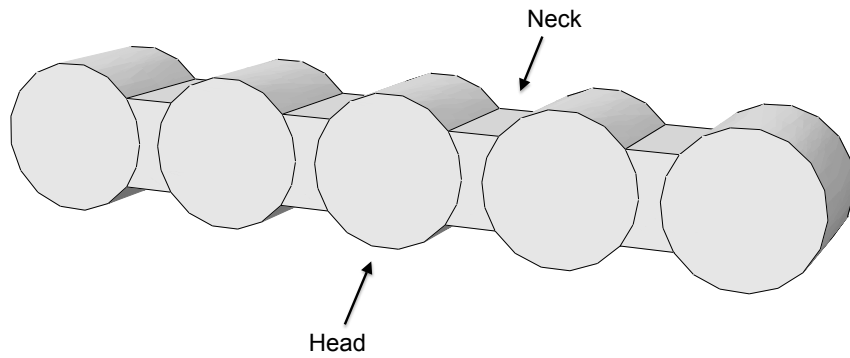


Figure 3.7: Metallock key part in Abaqus.

3.3.3 Metallock Screws

The geometry of the Metallock screws was simplified in the modeling by ignoring the screw threads. The modeled screw has the shape of a plain cylinder with a diameter of 6 mm and a length of 12.5 mm, which makes the screws penetrate the two top keys in the joint. The same material properties as for the parts of the Metallock keys unaffected by cold working were used for the screws. To avoid rigid body motion, springs with a stiffness of $k = 100$ kN/m were attached in three points in the x -, y -, and z -directions respectively on each screw.

For the specimen where the joint is inclined 45° to the load direction, the Metallock screws along the joint were neglected for simplicity.

3.3.4 Gray Cast Iron Components

The gray cast iron material was modeled in Abaqus using the built-in function *cast iron plasticity*. The input for this plasticity model is the plastic Poisson's ratio (which defines the inelastic volume change in tension, here assumed to be equal to the elastic Poisson's ratio) and the plastic behavior in tension and compression. Since gray cast iron practically lacks an elastic region in the stress-strain relation, plastic deformation starts more or less instantly when a load is applied on the material.

3.3.5 Residual Strain Simulation

The Metallock keys are hammered into place in the installation of the joint and this gives rise to residual strains in the keys as well as in the surrounding cast iron material. To simulate the residual strains an analysis was performed in Abaqus using a model with symmetric key arrangement in which each key was pressed down into the hole a distance of 0.03 mm, which makes a total of 0.12 mm for the four keys in each hole. When the keys are pressed down and compacted in their holes they expand in the other directions which creates a distribution of stresses in the surrounding gray cast iron component. The thickness of the keys were adjusted to 6.28 mm which made them fit perfectly with the height of the surrounding gray cast iron after the simulated hammering. The simulated hammering was performed in the same order as the real hammering, i.e. it began with the first layer in each hole and henceforth the same procedure was executed for the following layers. Each key was installed in a separate step to mimic the real installation procedure.

In the model symmetry was used according to Figure 3.8, to reduce the number of elements and thereby simplify the computation. The consequence of this is that the model

of the Metallock key installation is unable to simulate the real order in which the keys are installed. Using the symmetry means that the keys instead are inserted two at a time, symmetrically around the center of the mid key.

To prevent rigid body motion in the Abaqus models, which occurs if the analysis lacks essential boundary conditions, the Metallock keys and screws were connected with springs in three points on each component. The springs were applied in x -, y -, and z -directions, with a stiffness of $k = 100$ kN/m. The results from the residual strain simulations are presented in Section 4.2.1.2.

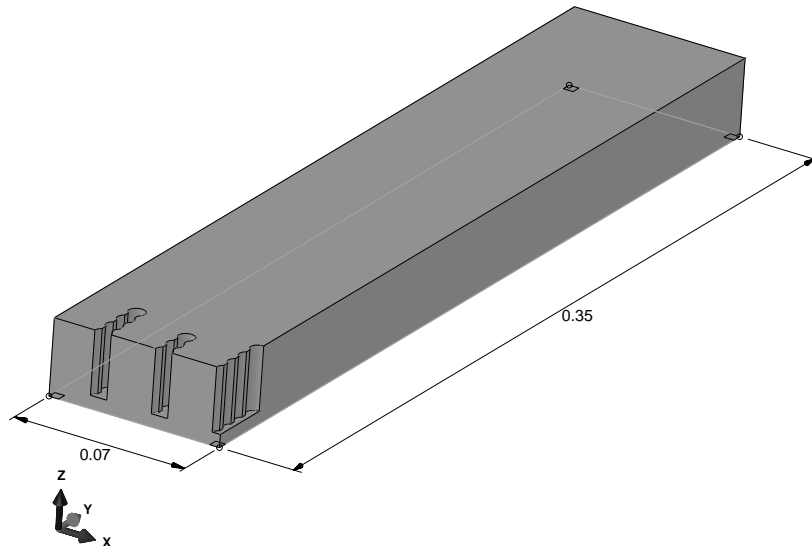


Figure 3.8: Symmetric FE-model in Abaqus where the symmetry plane is the yz -plane [m].

3.3.6 Contact Modeling and Friction

For the contact modeling the *general contact* algorithm with *interaction property* and the option *all* with self* was used, which automatically detects all surfaces that are in contact with each other and assigns appropriate master and slave surfaces. Friction was assigned to the contact areas as *tangential behavior* with *penalty contact* and the friction coefficient was estimated as $\mu = 0.17$ between the materials in contact, i.e. gray cast iron — iron–nickel alloy and iron–nickel alloy — iron–nickel alloy.

3.3.7 Boundary Conditions

For the models of the joints with straight key arrangements (7-5-7-5-7 and 7-5-7-5, described in Section 3.2.2.1 and Section 3.2.2.3) fixed boundary conditions at the symmetry plane through the Metallock keys were used. This was done by preventing all displacements (i.e. by setting $U1 = U2 = U3 = 0$ in Abaqus) in the section of the keys that cuts through the joint, see Figure 3.9. In all the models the load was applied at the top of the gray cast iron block as a negative pressure load.

Since no symmetry conditions were utilized in the model of the 45° inclined joint (see Section 3.2.2.2), the *encastre* condition in Abaqus (i.e. $U1 = U2 = U3 = UR1 = UR2 = UR3 = 0$) was instead used at the surface of one of the outer ends of one of the gray cast iron blocks. The load was applied as a negative pressure load at the surface of the free end of the other gray cast iron block.

In the residual strain simulation of the straight joint with 7-5-7-5-7 arrangement (see Section 3.2.2.1), the symmetry plane through the Metallock keys (as in Figure 3.9) was

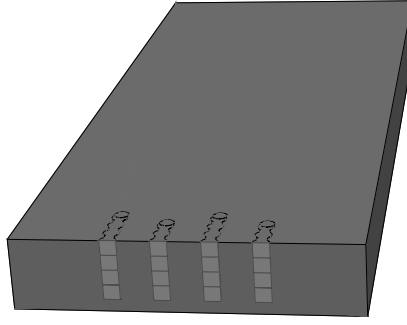


Figure 3.9: Light gray areas of the keys shows where the fixed boundary condition of the Metallock keys was applied.

modeled, by preventing displacements in the y -direction and rotations in the x - and z -directions (i.e. $U_2 = UR_1 = UR_3 = 0$ in Abaqus), and additional symmetry was used in the yz -plane (see Figure 3.8) where displacements in the x -direction and rotations in the y - and z -directions were prevented (by setting $U_1 = UR_2 = UR_3 = 0$). During the residual strain simulation the back of the block was fixed to simulate that the block was kept in a vise during the installation of the joint. This was done by prescribing all displacements on the back of the block to zero (i.e. $U_1 = U_2 = U_3 = 0$). Additionally, during the simulation of the hammering each key was pushed in separately (as described in Section 3.3.5). In addition all keys that had not yet been hammered were fixed to prevent rigid body motion.

3.3.8 Parametric Study

Since it is possible that the composition of the Metallock joint can be improved, the influence of changing different parameters of the joint were investigated. Two parameters were studied; the length of the keys and the distance between the keyholes.

3.3.8.1 Key Length

In order to further investigate the importance of the length of the Metallock keys for the load carrying capacity of the joint, two models were created — one with an ordinary 7-5-7-5 arrangement of the keys, and one with a 9-7-9-7 arrangement. The joints were modeled as typical “standard” joints in the same kind of gray cast iron blocks, with a size of $140 \times 30 \times 350 \text{ mm}^3$ as used in the DIC testing.

Both joints were subjected to a load of $F_y = 100 \text{ kN}$ and the maximum stress and strain magnitudes were compared. The results are presented in Section 4.2.4.1.

3.3.8.2 Distance Between Keyholes

Two models of specimens of the same type as in the experimental testing were created with different distances between the keyholes. Otherwise, the models were identical with four keyholes (7-5-7-5 arrangement) and Metallock screws at the end of each keyhole. Both models were subjected to a tensile load of $F_y = 100 \text{ kN}$ and the resulting ε_y strain fields were compared. The results are presented in Section 4.2.4.2.

4 Results and Discussion

4.1 Material Testing Results

The experimental results from the material testing are primarily used in the computational modeling of the Metalock method as described in the previous section. In this section the results from material testing of the Metalock keys and the gray cast iron components are presented and discussed.

4.1.1 Analysis of Chemical Composition

The result from the analysis of the chemical composition shows that the Metalock keys are made of an iron–nickel alloy, see Table 4.1. The results resembles a common iron–nickel alloy containing 36% nickel (and small quantities of manganese, silicon and carbon — totally less than 1%) called Invar, which has got its name from its low coefficient of thermal expansion that makes it practically invariable for ordinary temperature changes [4].

Using a material with thermal properties similar to Invar in the Metalock keys has potential effects on the mechanical behavior of the Metalock joint if subjected to large temperature variations, since it is likely that the gray cast iron has a higher coefficient of thermal expansion than Invar.

Table 4.1: Chemical composition of the Metalock keys.

Element	Method	Content [wt%]
Iron, Fe	-	~ 59
Carbon, C	IR Detection	0.039
Sulfur, S	IR Detection	0.005
Aluminum, Al	XRF	~ 0.2
Silicon, Si	XRF	~ 0.05
Manganese, Mn	XRF	~ 0.3
Cobalt, Co	XRF	~ 0.07
Nickel, Ni	XRF	~ 40
Copper, Cu	XRF	~ 0.2
Zirconium, Zr	XRF	~ 0.1

4.1.2 Dilatometric Analysis of the Metalock Keys

Figure 4.1 shows the measured thermal strains of the iron–nickel alloy in the temperature interval $T = 30^{\circ}\text{C}$ to $T = 450^{\circ}\text{C}$, and Figure 4.2 shows the corresponding coefficient of thermal expansion, α . It can be noted that the thermal strain plot has a negative slope from $T = 30^{\circ}\text{C}$ to $T = 250^{\circ}\text{C}$, corresponding to negative coefficients of thermal expansion in this range. In the interval $T = 100^{\circ}\text{C}$ to $T = 200^{\circ}\text{C}$ the mean value of the coefficient of thermal expansion can be estimated as approximately $\bar{\alpha} \approx -5 \cdot 10^{-6} \text{ K}^{-1}$.

The physical plausability of the results presented in this section are questionable. There are materials which shrink when heated, but usually only at low temperatures (0-100 K) [15]. More tests, possibly using other measurement techniques, are needed to confirm the results presented in this section.

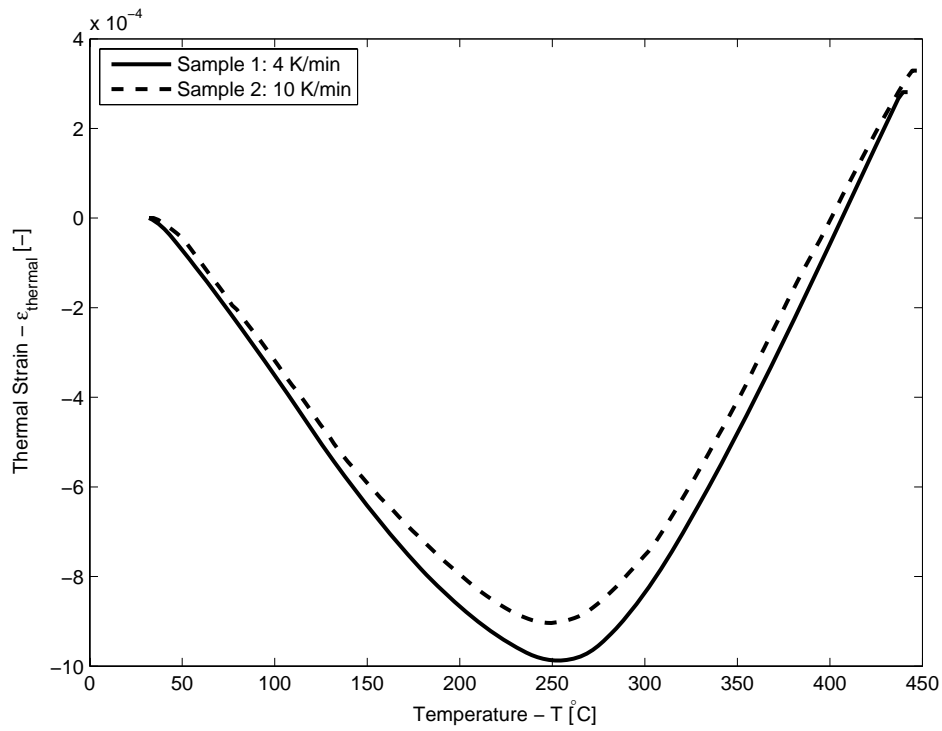


Figure 4.1: Measured thermal strains at temperatures from 30°C to 450°C.

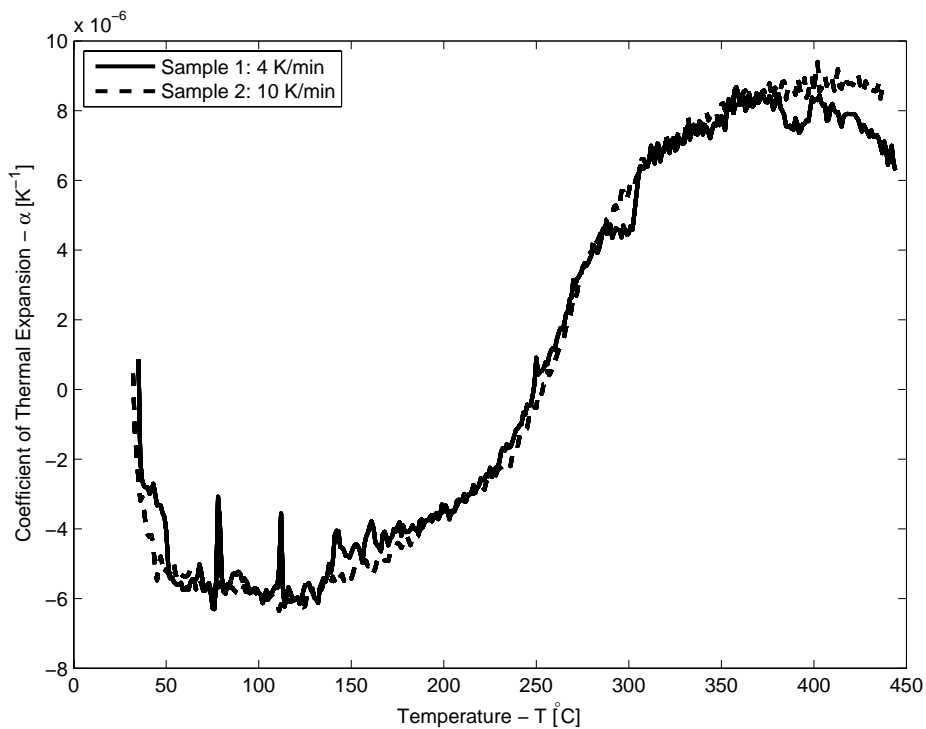


Figure 4.2: Coefficient of thermal expansion, α , at temperatures from 30°C to 450°C.

The test specimens used in the dilatometric analysis were cut out from Metalock keys, which have shown to have regions of cold worked material (see Section 4.1.5 and Section 4.1.7.1). According to the theory on strain hardening, cold working should increase the thermal coefficient of expansion, see Section 2.5. The importance of the cold working for



Figure 4.3: One of the tested specimens.

Table 4.2: Material properties of the iron–nickel alloy obtained from tension tests.

Engineering property	Sample 1	Sample 2	Mean
Yield strength, σ_o [MPa]	450.5	464.0	457.3
Ultimate tensile strength, σ_u [MPa]	534.5	542.0	538.3
Young's modulus, E [GPa]	148.4	135.8	142.1

the accuracy of the dilatometric measurement should be further investigated as a possible source of error.

A negative coefficient of thermal expansion (meaning that the material contracts in the temperature range of 30°C to 250°C) should have a significant effect on the mechanical behavior of the Metalock joint if subjected to large temperature variations. When the Metalock keys are contracting at the same time as the gray cast iron is expanding (assuming that it does), this means that the mended crack will be compressed, which could be considered as a beneficial effect. However, the contraction should also cause stresses, possibly of damaging magnitude.

4.1.3 The First Tension Test of the Metalock Keys

By visual inspection of the tested specimens from the first tension test, see Figure 4.3, one can observe that the specimens have necked at several locations along their length. This implies that the material is not homogeneous, possibly due to cold working in the manufacturing process. Hence the results from the tension tests are not valid for the iron–nickel material as a whole. The stress–strain relation in Figure 4.4 and the inelastic material parameters in Table 4.2 must therefore be considered as average values over the gauge length of the extensometer. Further analyses of the iron–nickel alloy are needed in order to obtain proper material data, such tests are presented in Section 4.1.8.

4.1.4 Tension Test of the Gray Cast Iron

Figure 4.5 shows the gray cast iron true stress–strain relationship, calculated using the mean nominal stress–strain values (according to Eq. 2.4 and Eq. 2.9) obtained from the tension test of the gray cast iron material.

Material parameters obtained in tension tests of the gray cast iron component are presented in Table 4.3. The tension tests shows that the material properties of the gray cast iron tested are way below that of the specification for a separate casting of C3Cu in Table 2.2.

Figure 4.6 shows the tangent modulus, E_t , for the gray cast iron material plotted as a function of the true strain, ϵ_{tr} . It is noticeable that the curve lacks an elastic region (which would have been represented by a horizontal line).

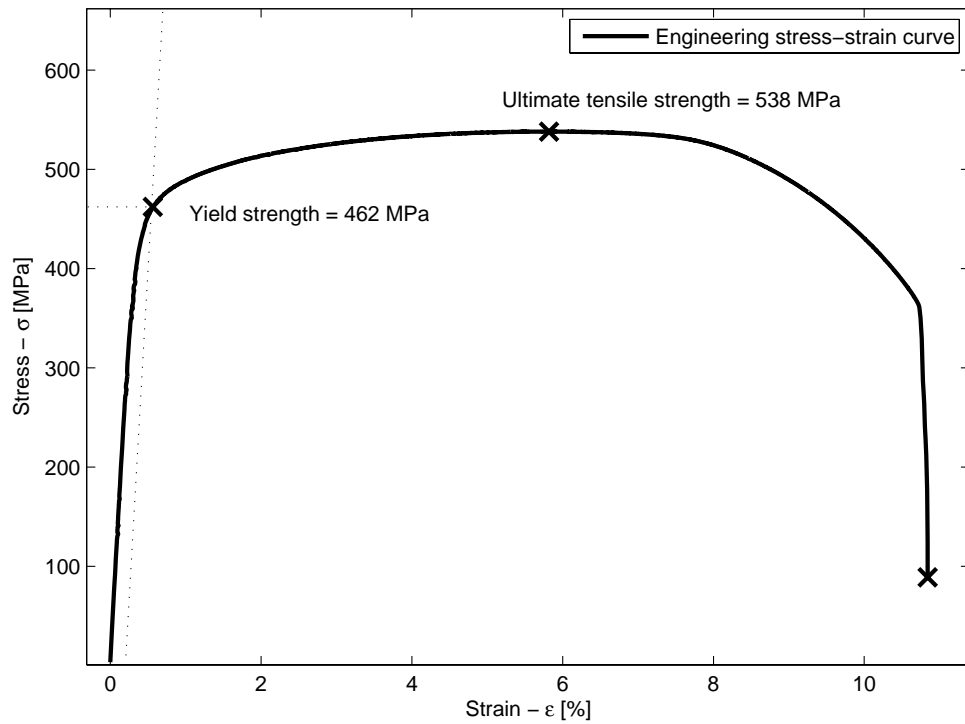


Figure 4.4: Nominal stress-strain relation obtained from the first tension tests.

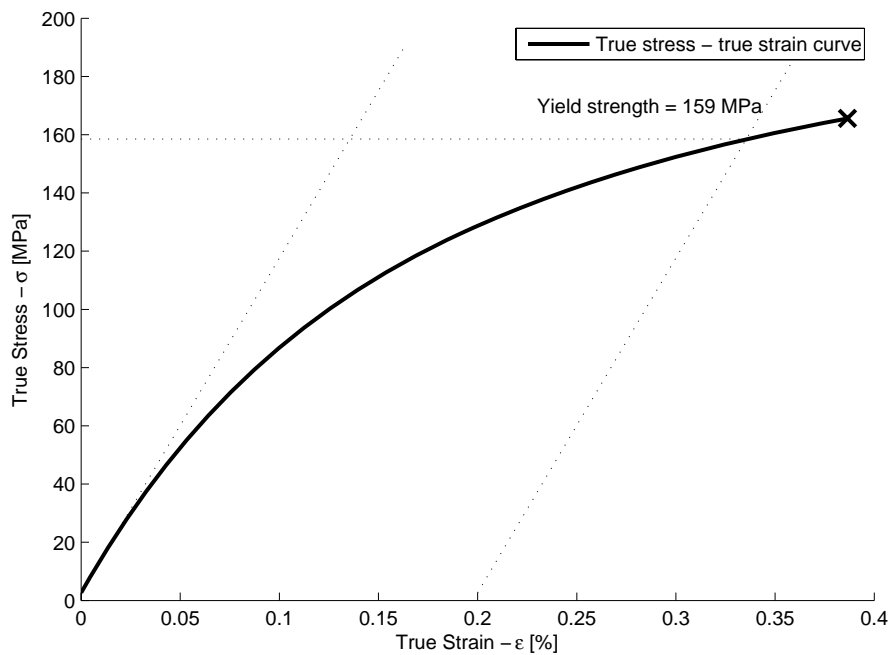


Figure 4.5: True stress-strain relation for the gray cast iron material.

Table 4.3: Material properties of the gray cast iron obtained from tension tests.

Engineering property	Specimen 1	Specimen 2	Mean
Tangent modulus, E [GPa]	118	118	118
Ultimate tensile strength, σ_u [MPa]	152.1	173.7	162.9
Yield strength, σ_o [MPa]	-	158.5	158.5

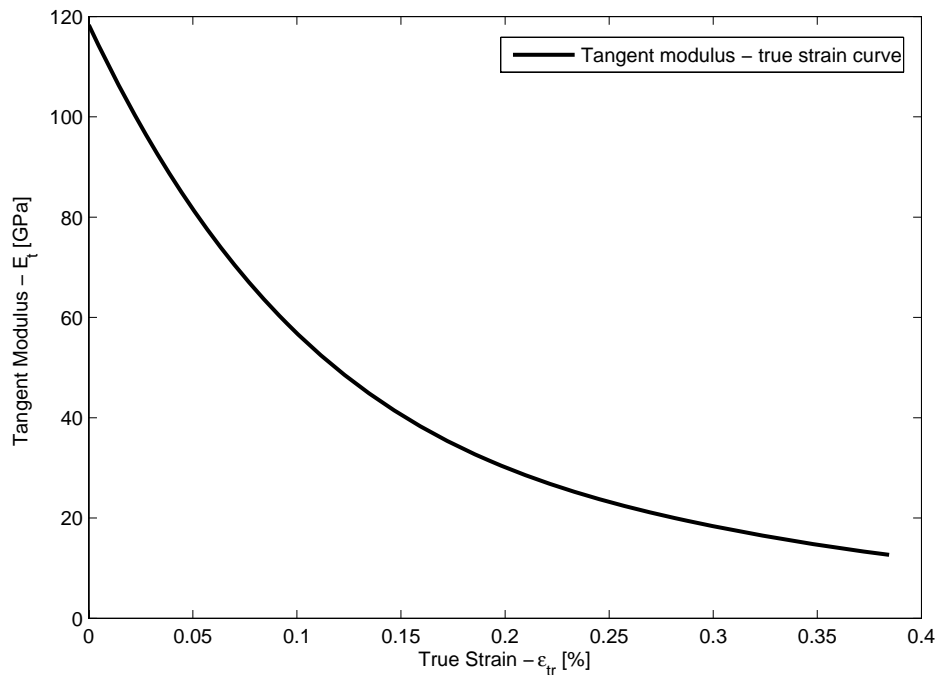


Figure 4.6: Tangent modulus–true strain relation for the gray cast iron material.

4.1.5 Hardness Test of the Metallock Key Material

The distribution of the hardness of a previously unused test specimen (i.e. it has neither been used in tension tests nor previously been used in a Metallock joint) can be seen in Figure 4.7, where indentations from Vickers test are visible as black marks in the top picture. It can be noted that the distribution of hardness seems to be related to the shape of the specimen — the neck regions have a significantly higher hardness number (HV) than the heads.

The blue areas inside the heads in Figure 4.7 can be assumed to represent the original hardness of the material while the increase of hardness between the heads indicates that the shape of the keys has been obtained by cold working, which has a strengthening effect and hence affects the hardness.

Figure 4.8 shows the result from a similar analysis on a previously used Metallock key. This specimen has fractured as a part of a Metallock joint in a previously performed tension test. The left side has a substantially increased hardness due to the plastic deformation and hardening in this zone prior to fracture. The well defined blue parts inside the heads as seen in Figure 4.7 are not as clear in this specimen. However, from $x = 15000 \mu\text{m}$ and forth, a similar pattern as seen in the unused specimen in Figure 4.7 is found. Furthermore, from the mosaic picture (the top picture in Figure 4.8) it can be noted that the two heads at the right end of the specimen are substantially deformed, indicating that they have carried load. Since the head to the left was situated in the middle of the joint, it has not been transferring any significant amount of load to the gray cast iron and is therefore mainly undeformed.

The difference in the hardness distribution between the used and unused specimens could to some extent be explained by the fact that the used specimen has been used in a Metallock joint and hence has been hammered which might cause the material to experience hardening. It can be concluded that the cold work process in the manufacturing of the Metallock keys is of importance for the mechanical behavior for the intended application.

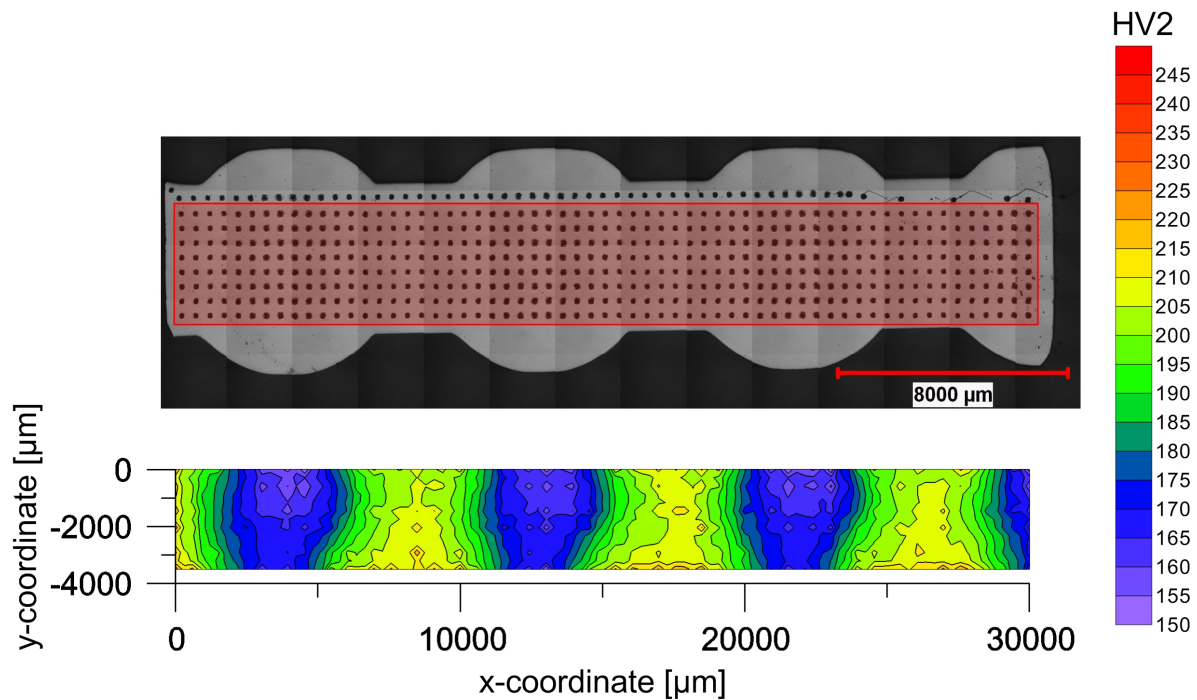


Figure 4.7: Unused specimen (top) and hardness distribution over this test specimen (bottom).

Figure 4.9 shows the hardness distribution of one of the test specimens from the tension tests in Section 4.1.3. When compared to Figure 4.7, it can be noted that the hardness distribution has a similar pattern apart from the fact that the hardness is more evenly distributed in the specimen. The regions with hardness numbers from $HV = 160 \text{ kg/mm}^2$ to $HV = 175 \text{ kg/mm}^2$ has disappeared, (the left part is unaffected since it is in the region of the grip), i.e. these areas of the tested specimen have hardened during the tension test. Since these areas have the lowest hardness and hence lowest yield strength this behavior can be considered reasonable.

When comparing the specimen in Figure 4.7 to the one in Figure 4.9, one must remember that the specimen tested in the tension test (Figure 4.9) has been machined and reshaped in order to create a uniform cross-sectional area. If the original shape of the Metallock key had been preserved, the hardness after a tension test might have had a different distribution since the irregular shape possibly would have affected the stress flow throughout the specimen.

Altogether, the Vickers tests show that the distribution of hardness and therefore also the yield strength varies in the material. This is clearly due to the cold working in the manufacturing process. The results from the tension tests in Section 4.1.3 might hence not be representative for the material in general. Therefore, further investigations, in terms of DIC aided tension tests, are of interest in order to more precisely determine the mechanical properties of the Metallock keys. Such tests are presented in Section 4.1.8.

4.1.6 Hardness Test of the Gray Cast Iron

The results from the hardness tests of the gray cast iron material are presented in Table 4.4. The mean value of the two specimens is 179 kg/mm^2 , which is considered reasonable compared to tabular values of similar gray cast irons [3].

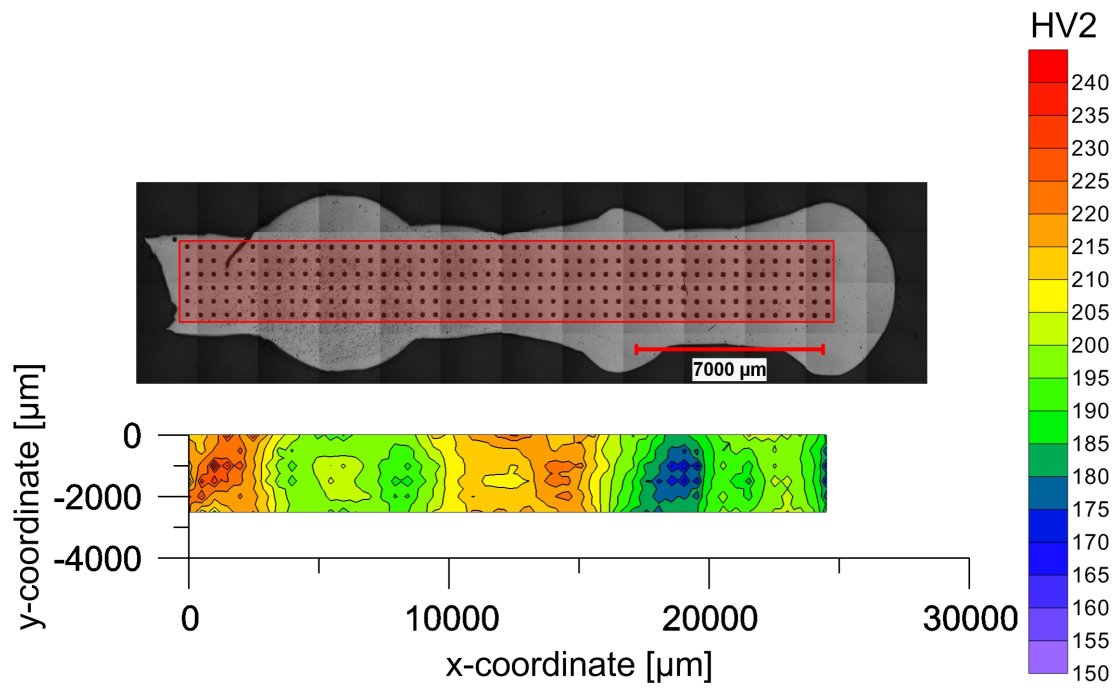


Figure 4.8: Used specimen (top) and hardness distribution over this test specimen (bottom).

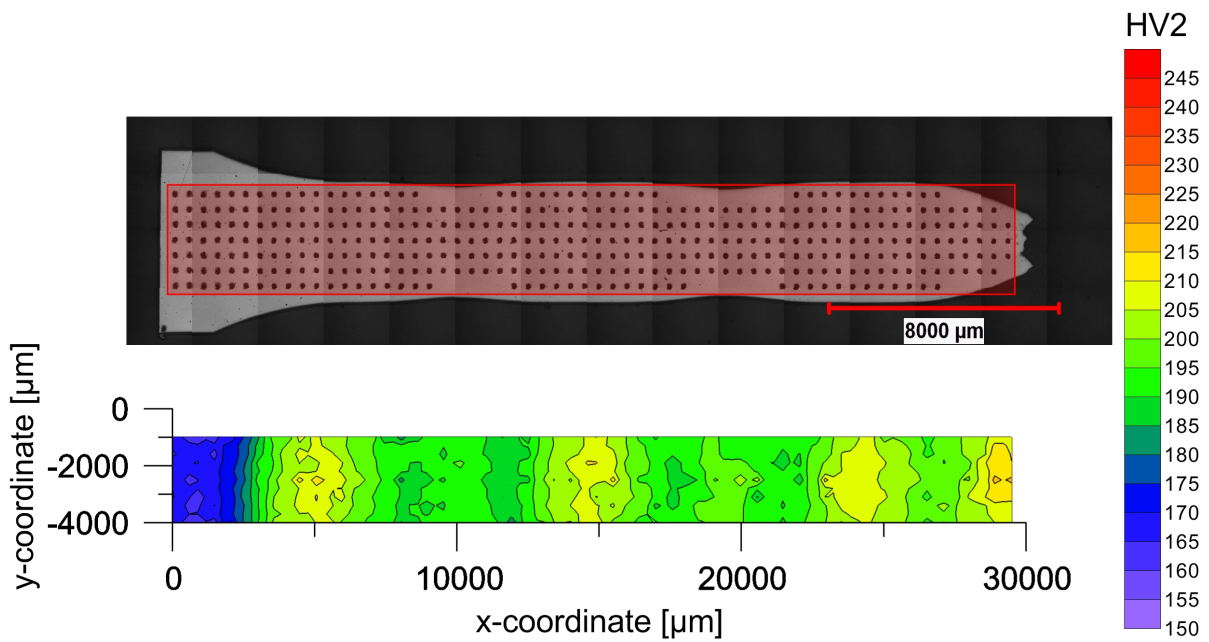
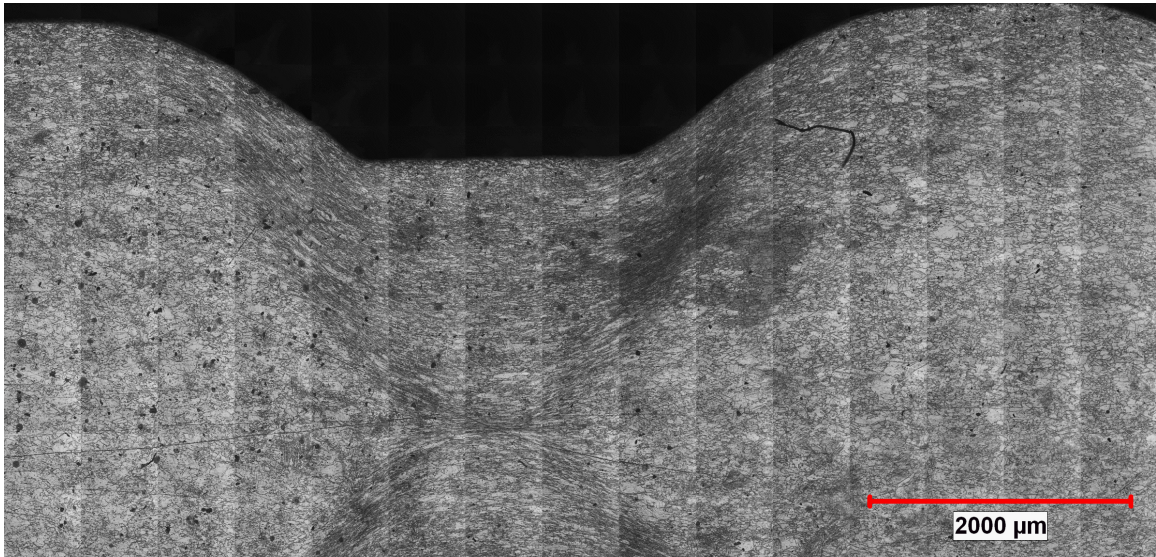


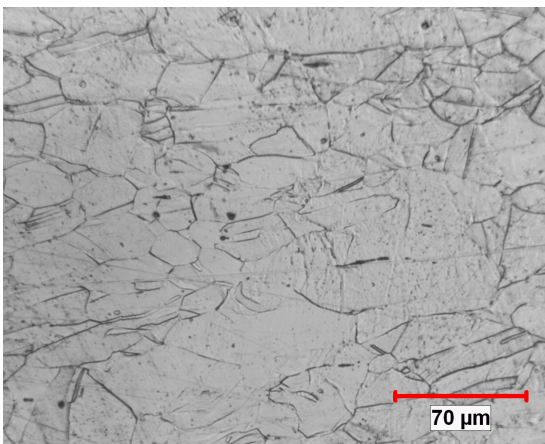
Figure 4.9: Specimen tested in tension (top) and hardness distribution (bottom).

Table 4.4: Hardness properties, HB [kg/mm²], of the gray cast iron material.

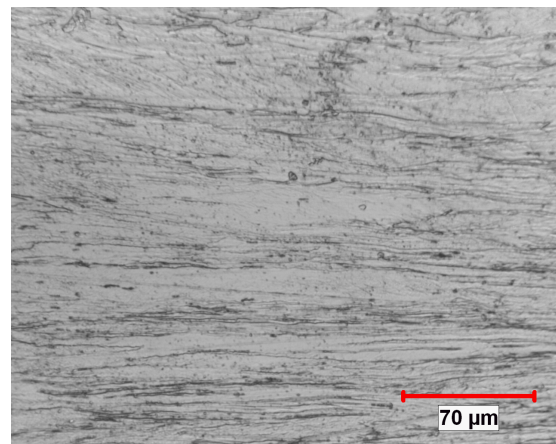
Specimen	Indent 1	Indent 2	Indent 3	Mean
1	179	176	173	176
2	195	179	172	182



(a) Etched surface in the area between two heads of the previously unused specimen.



(b) Grains in the Metallock keys unaffected by the cold working.



(c) Flattened grains in the middle of the neck of the specimen.

Figure 4.10: Microstructure of the nickel alloy in the Metallock keys.

4.1.7 Microscopic Analysis

In this section microscopic analyses of the different materials are presented.

4.1.7.1 Microstructure of the Metallock Key Material

In Figure 4.10 the microstructure of a Metallock key is shown. It is clear that the microstructure is varying in the same manner as the hardness, and that the material seems compacted in the areas between the heads. This further confirms the idea that the material has been cold worked in the manufacturing process and that this treatment has affected the material properties. The apparent differences in the material calls for a more sophisticated tension test in order to get an estimation of the varying stress–strain relation in the different regions.

4.1.7.2 Microstructure of the Gray Cast Iron Material

Figure 4.11 shows a mosaic (containing 36 images, each in $100\times$ magnification) of one of the etched gray cast iron specimens. In Table 4.5, the amount of graphite and the proportions of pearlite and ferrite for the gray cast iron material are presented.

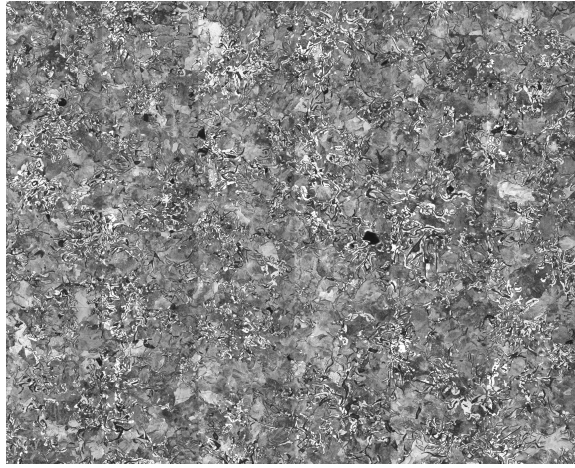


Figure 4.11: Mosaic of an etched gray cast iron specimen.

Table 4.5: Graphite and ferrite–pearlite proportions of the gray cast iron.

Sample	Graphite [%]	Pearlite [%]	Ferrite [%]
1	17.5	70.6	14.5
2a	15.0	74.8	12.1
2b	16.8	69.0	17.1

4.1.8 Refined Tension Test of the Metallock Keys Using DIC

The true stress–true strain relation of the parts of the Metallock keys unaffected by cold working is represented by the “original” curve in Figure 4.12. This curve is created using the mean values of the strength coefficient K and the strain hardening exponent n from the two tests, see Table 4.6. The yield strength, σ_o , is somewhat lower than in the first tension test, see Section 4.1.3. This is reasonable because the first tension test should be considered as a mean value over the extensometer length, which includes parts affected by cold working, and consequently results in a higher yield strength. It can be noted that the Young’s modulus in Table 4.6 is considerably lower (close to half) than that obtained in the first tension test. The reason is that the Aramis data were distorted in the elastic region, which made it difficult to measure the Young’s modulus in a proper way. Theoretically the Young’s modulus should not be affected by strain hardening and hence the value obtained in the first tension test is considered to be reliable.

Figure 4.13 shows strain versus time at five points where the largest strains were measured in one of the specimens using DIC. In the color plot, the variation in strain for the different parts of the specimen is visible. The parts affected by cold working show almost no measurable strain.

As described in Section 3.2.1 the material parameters of the hardened parts of the

Table 4.6: Material properties of the iron–nickel alloy obtained from tension tests.

Engineering property	Specimen 1	Specimen 2	Mean
Young’s modulus, E [GPa]	74	70	72
Ultimate tensile strength, σ_u [MPa]	539	538	539
Yield strength, σ_o [MPa]	440	390	415
Strength coefficient, K [MPa]	829	867	848
Strain hardening exponent, n [-]	0.139	0.158	0.149

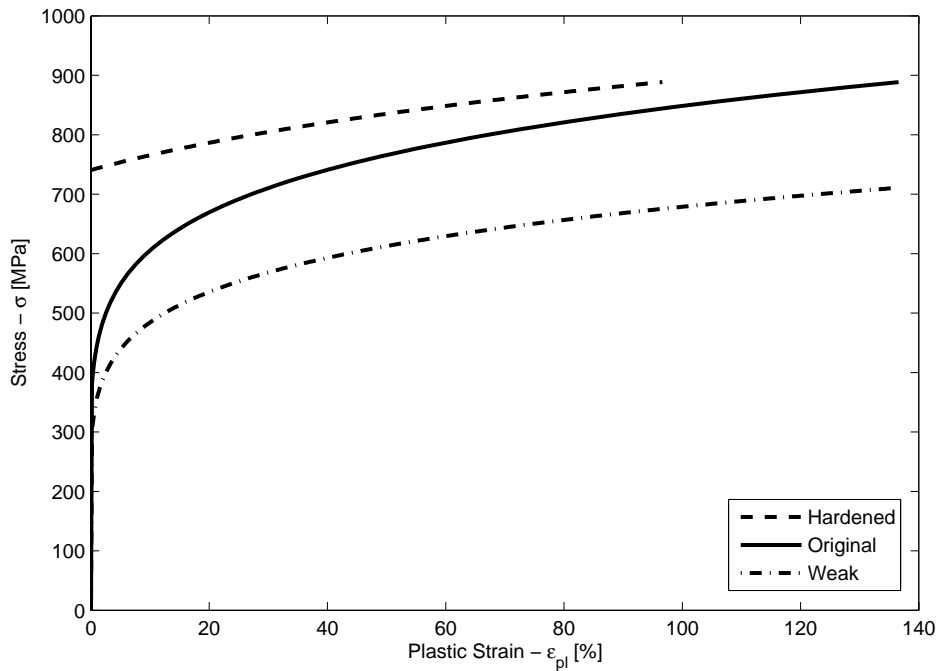


Figure 4.12: Different stress–strain relations obtained for different calibrations of the material model parameters.

Metallock keys were determined by calibration of model parameters. Figure 4.14 shows a comparison of the strain versus section length from the Aramis tests and the Abaqus simulations with tuned material parameters using the iterative procedure as described in Section 3.2.1. Figure 4.14b shows the Abaqus simulation where the hardened parts have an increased yield strength, which was found by iteration to be about 741 MPa (this curve is represented by the “hardened” curve in Figure 4.12). The weak part in the middle of the section length is modeled using the stress–strain relation represented by the “weak” curve in Figure 4.12. The measured and simulated strain versus section length shows a satisfactory correlation and the material properties used are considered appropriate.

In Figure 4.14 it can be noted that the distance between the local maxima differ somewhat between the experimental data and the simulated result. It is however not considered to significantly affect the overall response. It is also important to underline that the calibrated material properties should be considered an approximation due to the many uncertainties in the calibration method used.

4.2 Metallock Joint Testing and Simulation

The results from the tests and simulations of the Metallock joints are primarily presented in strain plots and load–displacement graphs. The tested and the simulated results are compared and discussed in this section. Additionally, the results from the parametric study of the Metallock joint are presented and discussed.

4.2.1 Joint with Symmetric Key Arrangement

The joints with symmetric key arrangement were subjected to different load schemes and measured using different measuring volumes. The results from the different tests and simulations, as well as from the residual strain simulation, are presented in this section.

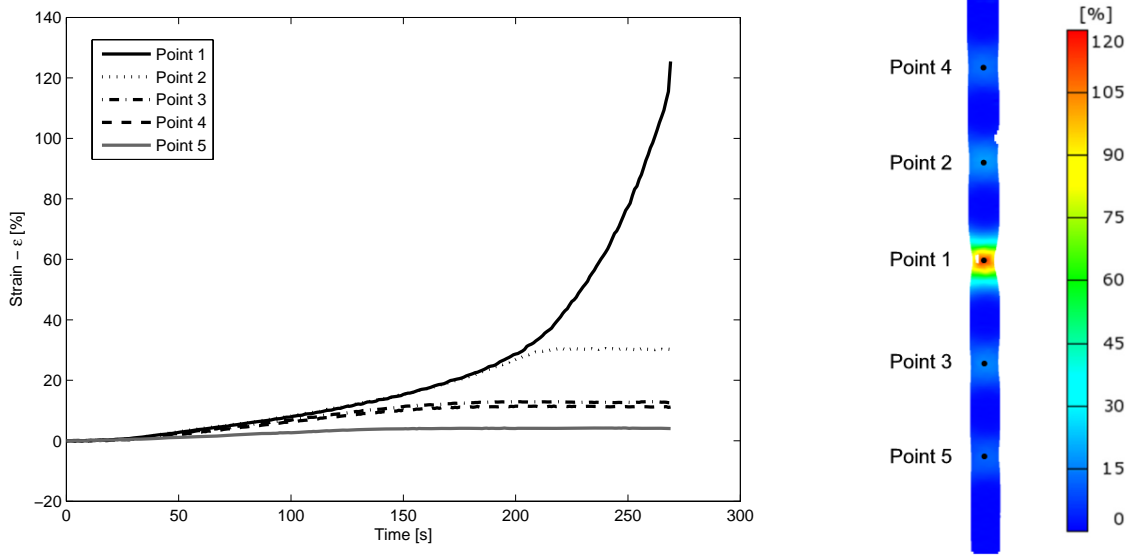


Figure 4.13: Strain versus time at five points (left) and an Aramis color plot of the tested specimen (right).

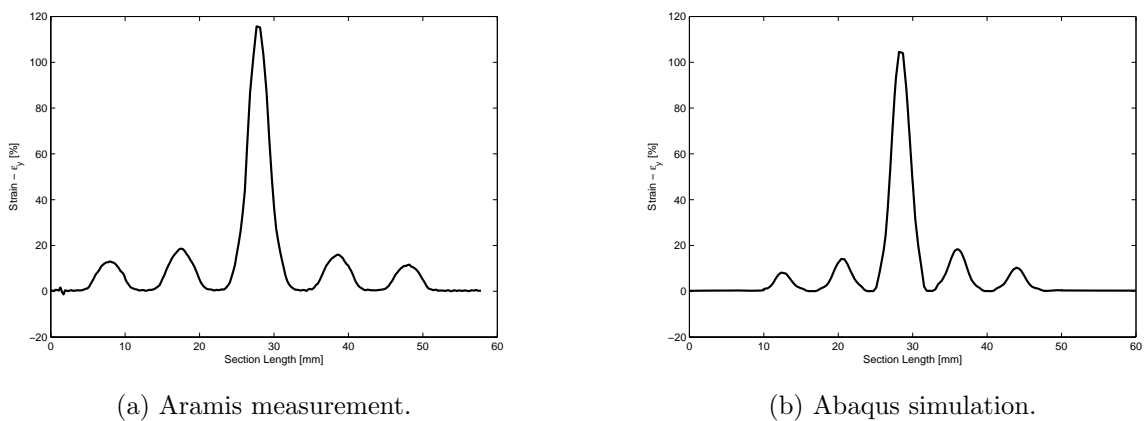


Figure 4.14: Strains in the mid-section of the test specimen.

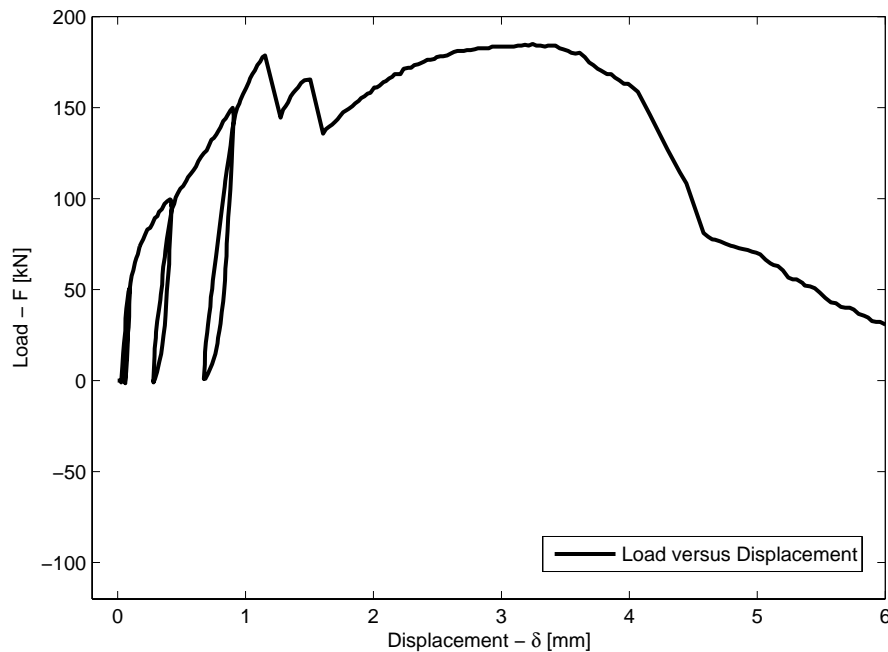


Figure 4.15: Load versus displacement relation for the symmetric Metallock joint without screws in cyclic tension.

4.2.1.1 Cyclic Tension

Figure 4.15 shows the measured global load versus displacement relationship, obtained by placing a virtual extensometer measuring point on both gray cast iron blocks, at the ends of the middle keyholes in the cyclic tensile test (see Figure 4.16 where the virtual extensometer is shown as an double sided arrow). The original distance between the points was $L_0 \approx 61$ mm, and the displacement δ_y was measured as the difference in length, i.e. $\delta_y = L - L_0$. It is seen in Figure 4.15 that the load–displacement relation is becoming nonlinear at $F_y \approx 60$ kN.

At $\delta_y \approx 1.2$ mm, corresponding to $F_y \approx 179$ kN the gray cast iron component cracked and failed at the right outermost part, see Figure 4.16. This can be seen in Figure 4.15 as the first sudden drop in load level. The second drop at $\delta_y \approx 1.5$ mm, and $F_y \approx 165$ kN is due to failure at the left outermost part of the cast iron component, see Figure 4.16. When the outermost parts of the gray cast iron component fails, the outer keys are no longer able to carry any load, so the load capacity from $\delta_y \approx 1.6$ mm up to the global maxima at $\delta_y \approx 3.2$ mm is hence achieved by the three middle keys.

If the distance from the outermost key to the edge of the specimen were greater, the initial cracking may never have taken place, which certainly would have resulted in a higher load carrying capacity of the joint.

Figure 4.16 shows the vertical strain field (i.e. ε_y) and the horizontal strain field (i.e. ε_x) respectively, prior to the first failure in the gray cast iron component, i.e. at the maximum load, $F_y \approx 175$ kN. The relatively coarse facet (subset) size used in the Aramis strain computation has the drawback of creating large voids in the masked areas in the edges around the Metallock keys (which also visually makes the proportions mismatch the FEM-models). The largest ε_y strains seems to be appearing at the ends of the longer keys, especially at the end of the right outermost key where also the first cracks developed. This is clearly due to boundary effects at the edge of the gray cast iron component, which causes bending of the outermost gray cast iron part when the joint is subjected to tension.

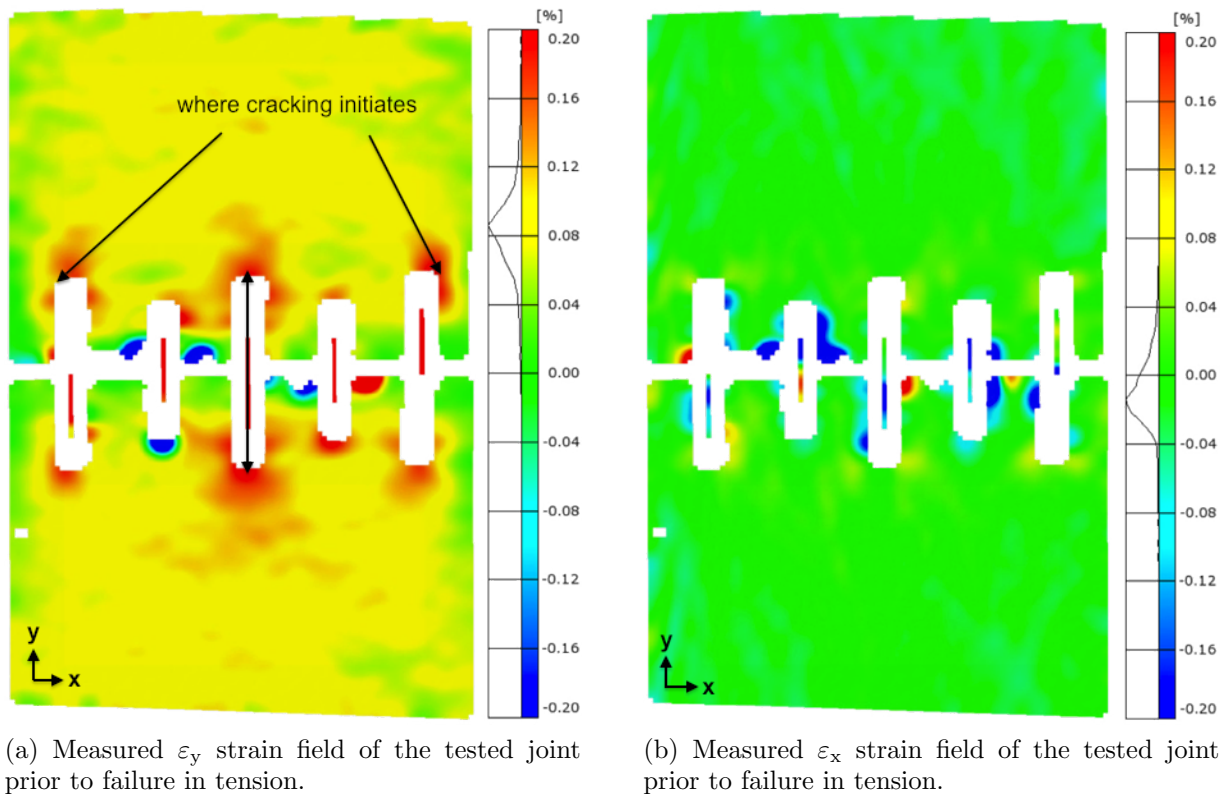


Figure 4.16: Measured strain fields in tension at $F_y = 175$ kN.

In Figure 4.16a, small fields of negative strains (suggesting compression) can be found at some locations. Since the Metallock keys do not penetrate the entire thickness of the gray cast iron component, a bending action is introduced that possibly could cause these zones of compression. Alternatively, and most likely, these negative strains originate from errors in the Aramis strain calculation.

Figure 4.17 shows the corresponding simulated response of the Metallock joint in pure tension. Figure 4.17b, displays the simulated ε_x strains, which predicts that the largest compression in the gray cast iron component should occur in the top heads of the shortest key components which in turn could indicate that the major part of the load at this moment is carried by these heads. The Aramis results in Figure 4.16b supports this theory to some degree in the sense that a large amount of the measured negative ε_x strains are located around the two shorter keys. However, due to the coarse facet size it is hard to draw any conclusions about this.

When comparing the experimental results to the simulations, the most significant difference is seen in the ε_y strain field at the top of each of the Metallock keys. In the Aramis measurement there seems to be a concentration of strains in these areas — while in the simulation the strains in the corresponding areas are practically zero. However, the model shown in Figure 4.17 does not include the residual strains that resulted from hammering of the keys in the repair process. Residual strains could be part of the explanation to the differences between measurements and simulations and the effect of these residual strains are analyzed separately in Section 4.2.1.2.

4.2.1.2 Residual Strains

Figure 4.18 shows the numerically predicted ε_y strain distribution around the Metallock keys prior to the tensile testing (note that the scale is different from that in Figure 4.17),

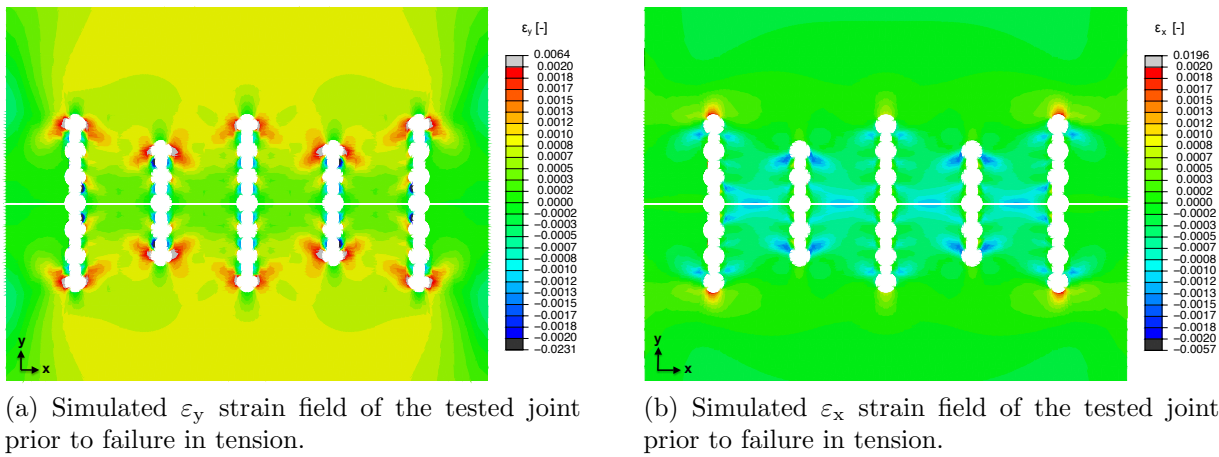


Figure 4.17: Simulated strain fields in tension at $F_y = 175$ kN.

where the Metallock keys have been pushed into their holes and where each of the keys have been forced in an additional 0.03 mm, creating a field of compressive strains mainly at the top of each key and some tensile strains mainly on each side of the top head of each key component. Figure 4.19 shows the strains after an additional load of $F_y = 175$ kN was applied. It can be noted that the compressive zones above the Metallock keys have decreased in size.

The results from the residual stress analysis gives a possible explanation of the differences between the Aramis results and the simulations, as discussed in Section 4.2.1.1. The Aramis calculations do not take into account any strain fields that are present in the material prior to the analysis. This means that the relaxation of the compressive strains in the Aramis analysis instead are interpreted as increased tensile strains.

In the Aramis measurement the ε_y strain magnitude at the top of each key are considerably higher than what is predicted in the residual strain simulation. An explanation could be that in the real Metallock repair process, the lower layers of keys may not be hammered as hard as the upper layers. It is even possible that it is only during the installation of the top layer that the keys are actually hammered to fit into their holes. In that case the residual strain distribution should be largest at the surface of the joint. It is also possible that the estimated distance of 0.03 mm per key is on the low side.

In summary, conclusions drawn from the residual strain analysis should be based on the shape of the strain field and not on local magnitudes.

In Figure 4.20 the measured strain field at $F_y = 100$ kN (Figure 4.20a) is compared to the measured strain field after unloading (Figure 4.20b). The remaining strains are located primarily in the areas above the ends of the keys. A possible explanation is that during loading, the residual compressive strains at the ends of the keys are reduced, and at $F_y = 100$ kN most of the residual strains have been relaxed. Upon unloading, at $F_y = 0$ kN, the only strains left are the relaxed residual strains which Aramis interprets as increased tensile strains.

4.2.1.3 Cyclic Tension — Higher Resolution DIC Measurements

Figure 4.21 shows the measured ε_y and ε_x strain distribution from a similar analysis as before but focused on a smaller region around two of the middle keys in the joint. Here, it is possible to see the strain distribution in the Metallock keys.

During the test when the joint was subjected to tension, it was observed that the Metallock keys in the outermost layer started to come out of their holes, see Figure 4.23.

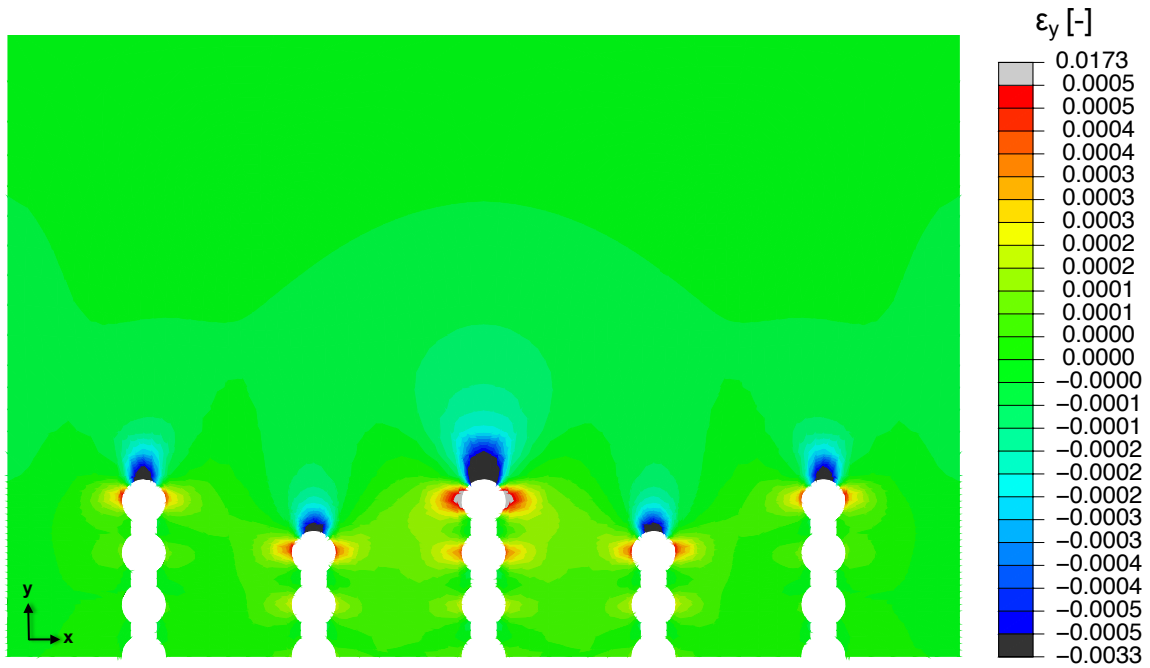


Figure 4.18: Numerically predicted ε_y strain distribution around the Metallock keys after they have been hammered into place.

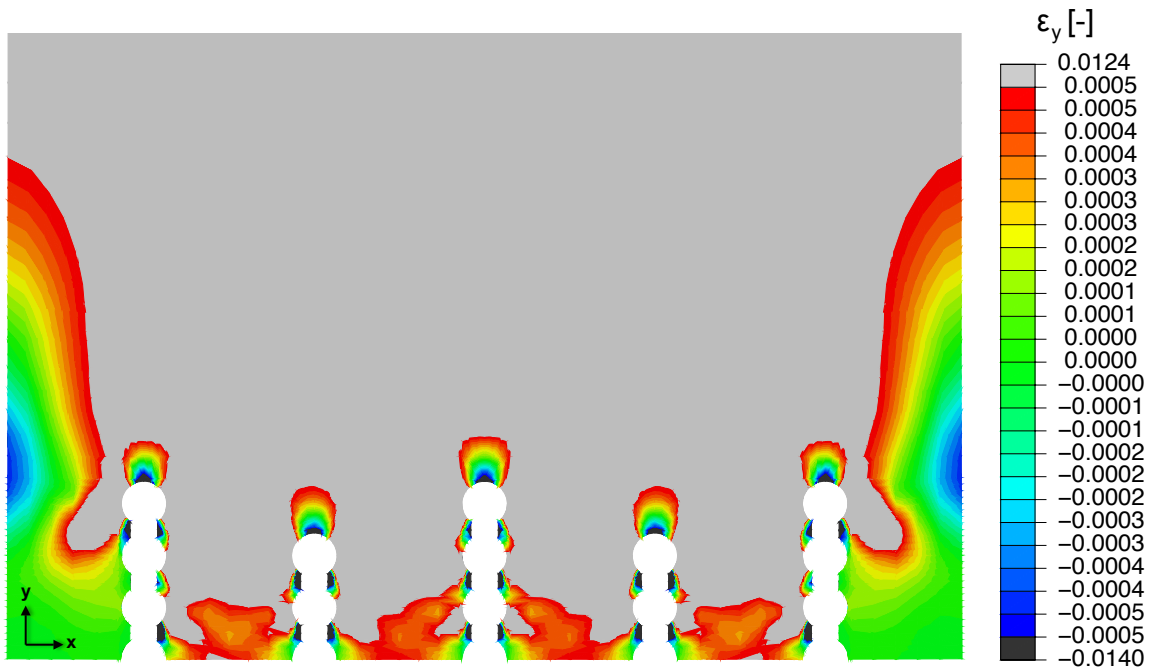
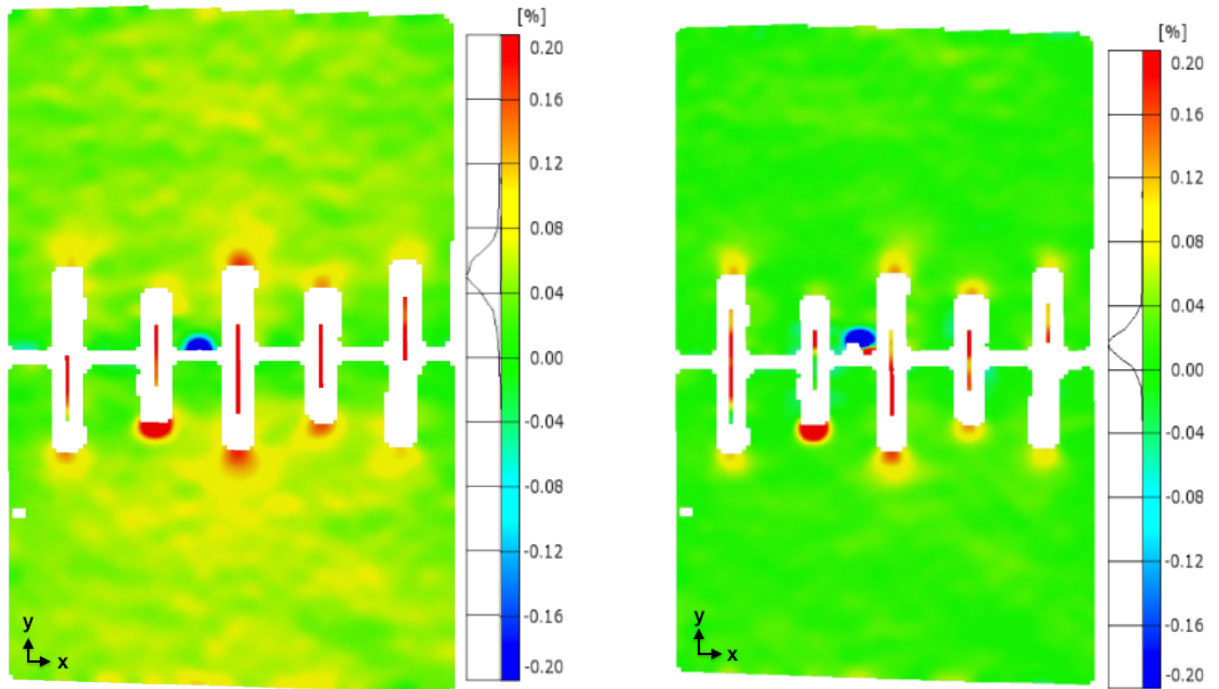


Figure 4.19: Numerically predicted ε_y strain distribution around the Metallock keys after they have been hammered into place and the joint has been subjected to $F_y = 175$ kN in tension.



(a) Measured ε_y strain field of the tested joint at $F_y = 100$ kN.

(b) Measured residual ε_y strain field of the tested joint after unloading.

Figure 4.20: Comparison of measured strain fields.

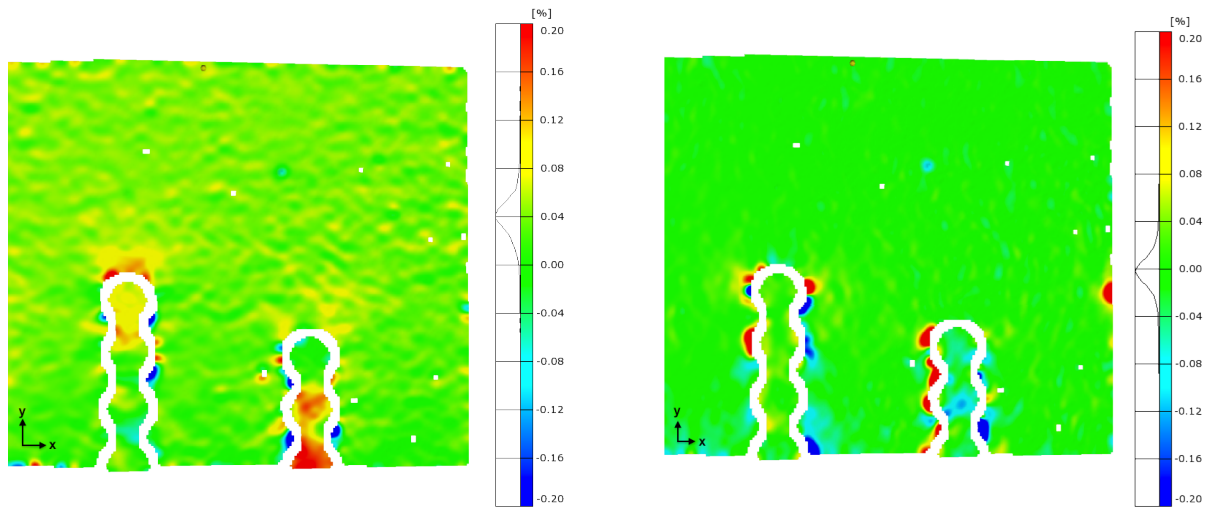
This behavior could possibly be enhanced by the fact that the surface of the joint had been milled about 0.5 mm, consequently reducing the thickness of the outermost keys. Because of this, the results in Figure 4.21 should be treated with caution. The fact that the Metallock keys came out of their holes indicates one possible purpose of the Metallock screws; namely to prevent this from happening.

Figure 4.22 shows the numerically predicted strain fields in the same zoomed in area as the measurements presented in Figure 4.21. In this simulation the residual strains from the hammering of the keys are not taken into account. When comparing the Aramis results to the Abaqus simulations in Figure 4.21b and Figure 4.22b respectively, it can be noted that the compressive strain fields have certain similarities. It seems as if the load is carried by all the heads of the Metallock keys as opposed to primarily being carried by one single head.

Figure 4.24 shows a comparison of the minimum principal strain fields from simulations to measurements, where the zones of compressive strains around the heads of the keys are visible in both figures. In these figures it is even more pronounced that the load is distributed on all the heads of the keys. This suggests that the length, i.e. the number of heads, of the keys is an important parameter in the Metallock method. If it can be assumed that all keys carry approximately the same amount of load, the FE-simulation indicates that the shorter key length yields a larger amount of concentrated compressive strains in the gray cast iron than the longer ones, which might suggest that longer keys should be preferred.

4.2.1.4 Cyclic Compression

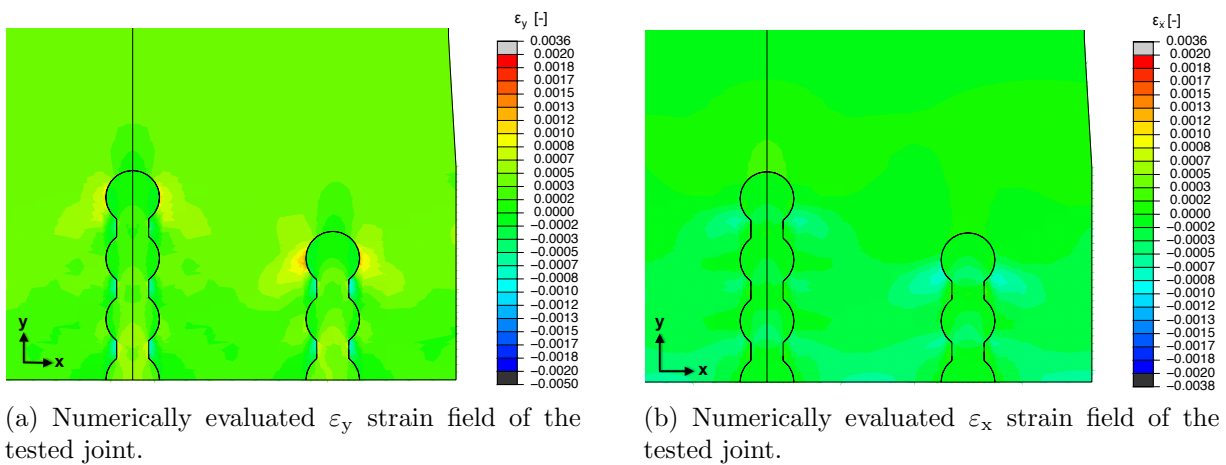
Figure 4.25 shows the measured global load versus displacement relationship for the symmetric Metallock joint tested in cyclic compression obtained in a similar manner as for specimen in Figure 4.15. Two points were placed on each side of the joint at the ends of



(a) Measured ε_y strain field of the tested joint.

(b) The ε_x strain field of the tested joint.

Figure 4.21: Measured strain fields in tension at $F_y = 87$ kN.



(a) Numerically evaluated ε_y strain field of the tested joint.

(b) Numerically evaluated ε_x strain field of the tested joint.

Figure 4.22: Simulated strain fields in tension at $F_y = 87$ kN.

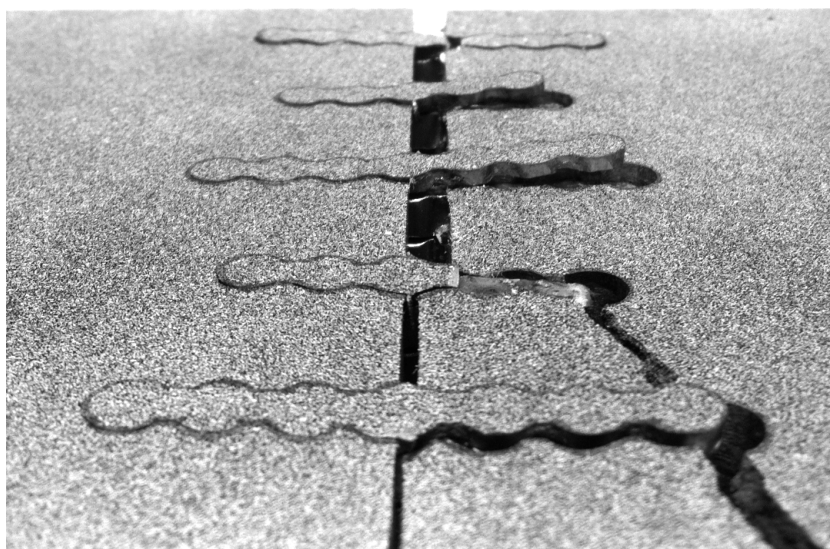


Figure 4.23: Picture of the failed component where it is visible that the top layers of the keys have come out of their holes.

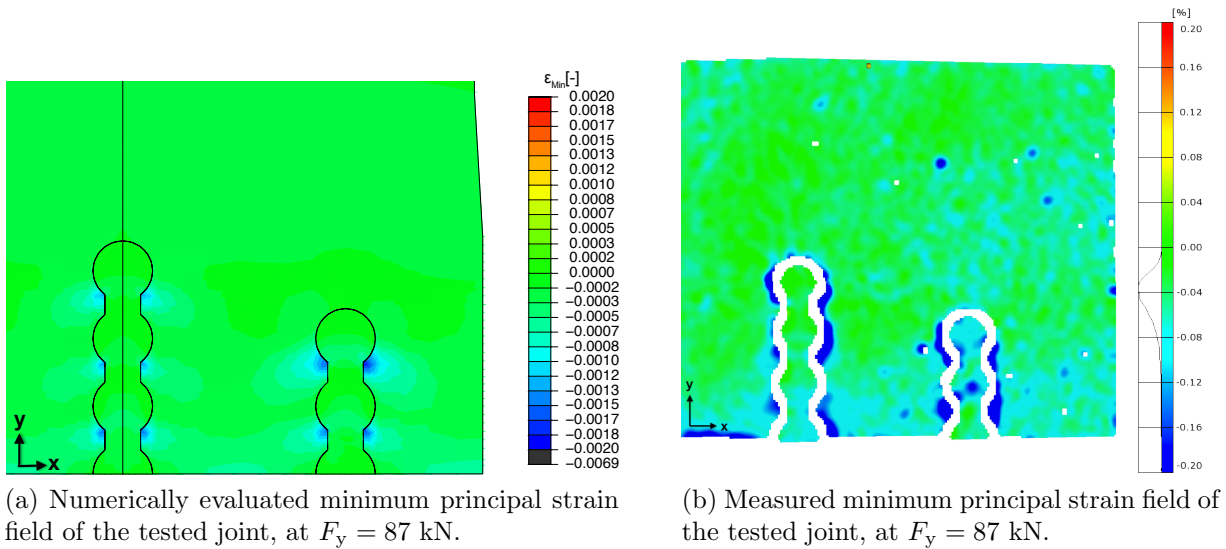


Figure 4.24: Comparison of (a) simulation and (b) measurement of the minimum principal strain.

the middle keyhole. The original length between the two points was again $L = 61$ mm in order to be able to approximately compare results. It can be noted that the load level at which the curve becomes nonlinear has decreased compared to the corresponding cyclic tension test (see Figure 4.15), from $F_y \approx 60$ kN to $F_y \approx 50$ kN. This could be an effect of the cyclic compressive loading but it could also be due to variations of the material quality in the keys or possibly in the gray cast iron.

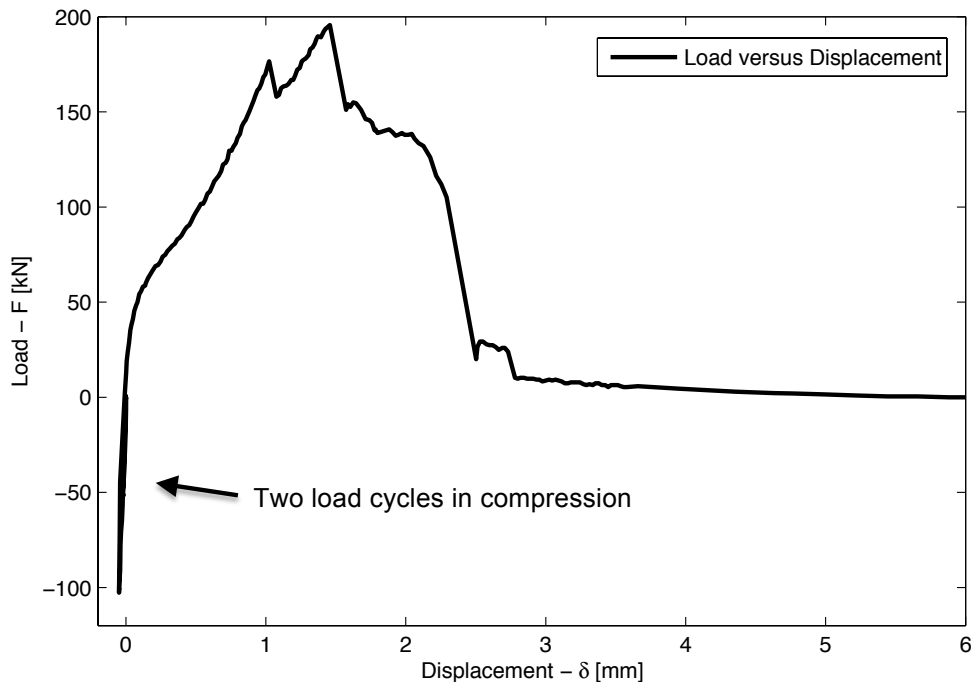


Figure 4.25: Load versus displacement for the symmetric Metallock joint without screws in cyclic compression.

Figure 4.26 shows the measured ϵ_y and ϵ_x strain fields at $F_y = -100$ kN, i.e. when the joint is subjected to compression. Since the gray cast iron has a higher stiffness in

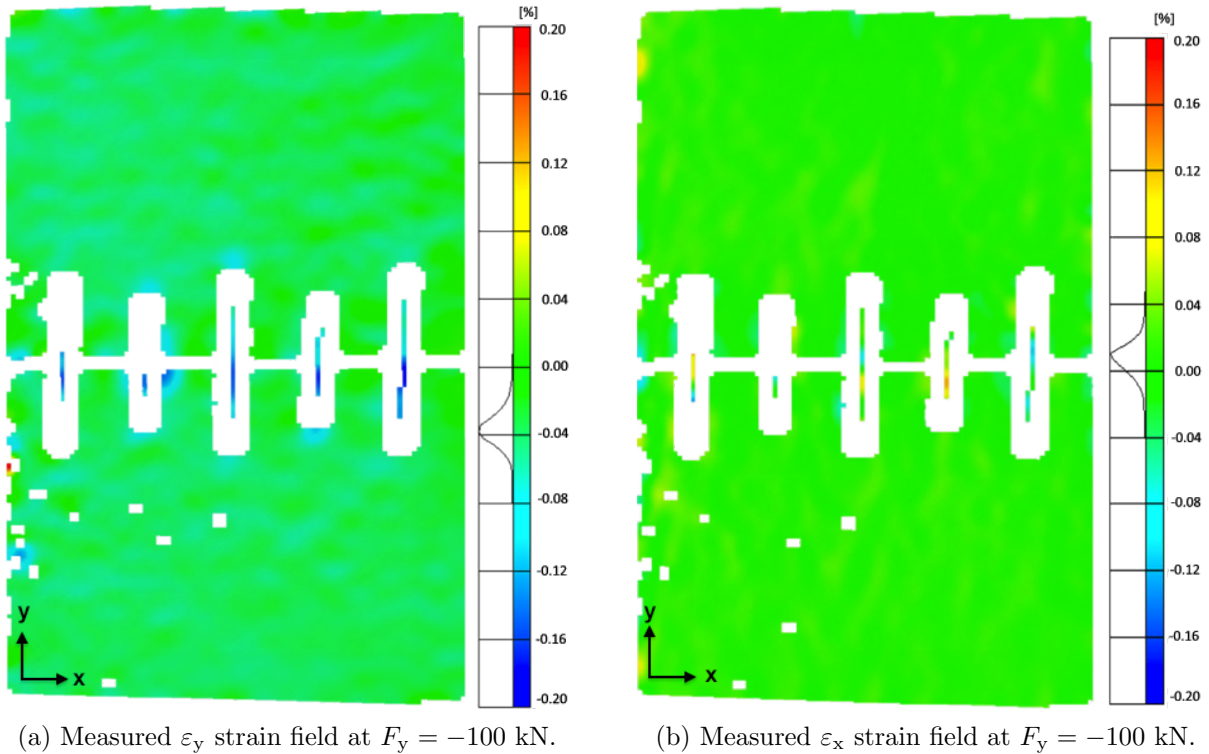


Figure 4.26: Measured strain fields in compressive loading.

compression than in tension the strain magnitudes are considerably lower than what was observed in the tension tests. Figure 4.27 shows the simulated response in compression. Again, the residual strains after hammering are not taken into account.

4.2.2 Cyclic Tension Test of Standard Joint with Four Keyholes

Figure 4.28 shows the measured global load versus displacement relationship obtained by placing a virtual extensometer between two points on each side of the joint as described previously. In this specimen nonlinear deformations are found above roughly $F_y = 80$ kN, which compared to the other specimens is rather high. In Section 4.2.1.1, the corresponding value was about $F_y = 60$ kN. That specimen had five keyholes corresponding to a total number of 20 Metallock keys, while this specimen consisted of only four keyholes

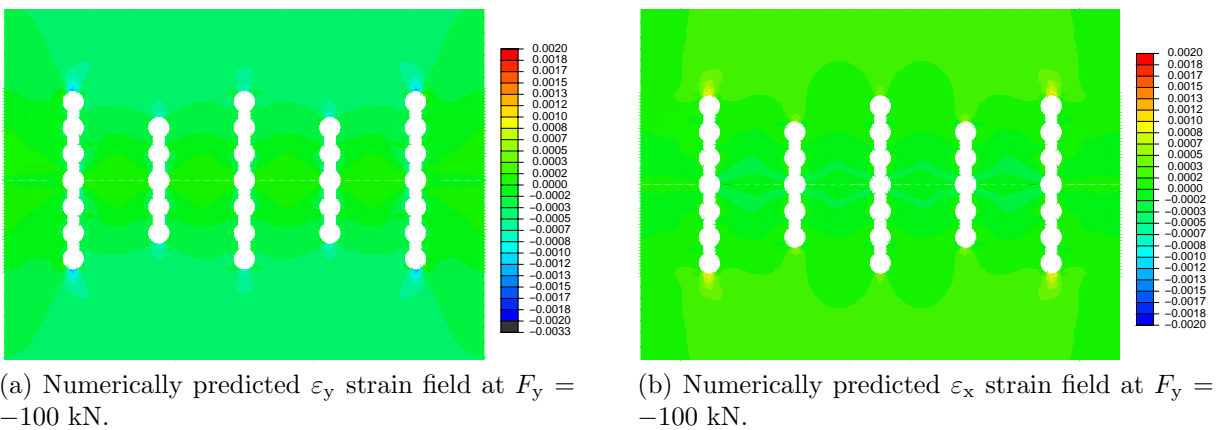


Figure 4.27: Simulated strain fields in compression.

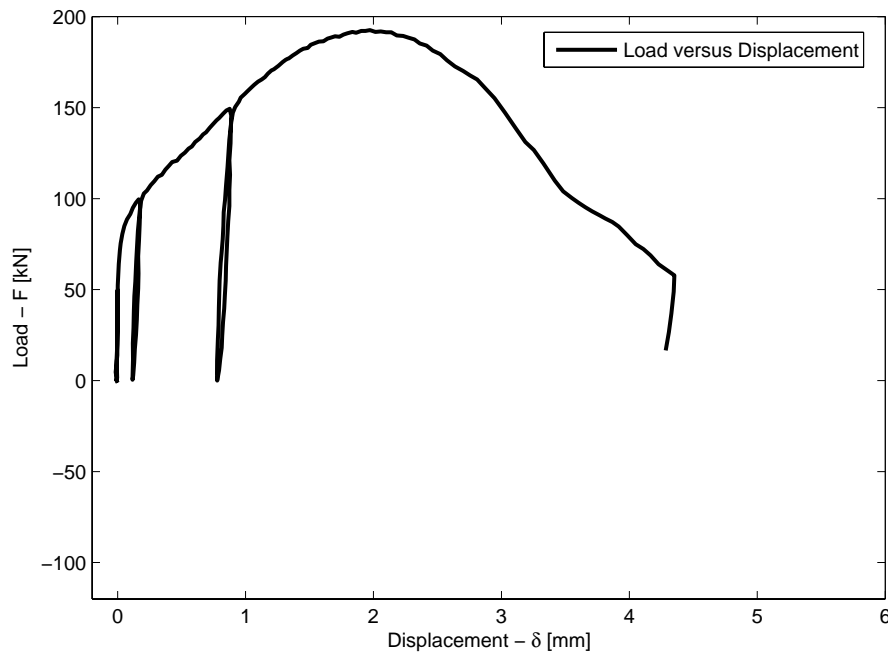


Figure 4.28: Measured global load–displacement relationship.

corresponding to 16 Metallock keys. In other words; the current joint seems to be stronger even though the joint has a lower number of keys. One possible reason for this is that in the specimens with five keyholes, the outermost parts of the gray cast iron were thin and therefore weak, which resulted in that they were bent (which eventually lead to failure in these parts) meaning that the outermost Metallock keys did not carry load to their full potential. It could thus be assumed that the two outermost keyholes and their keys did not contribute (much) to the load carrying capacity of the joint, meaning that in a worst-case scenario the load was carried by $3 \times 4 = 12$ Metallock keys instead of 20. In the current test however, no such behavior in the outermost gray cast iron parts is occurring which means that all 16 keys carry load to their full potential. This explanation is reasonable since the nonlinear behavior of the plot in Figure 4.28 starts at a load which is about $16/12 = 133\%$ of the corresponding load in Figure 4.15.

From Figure 4.28, it can be noted that in this specimen, no sudden drops in load level (cf. Figure 4.15 and Figure 4.25) were registered during loading which corresponds to the absence of failures in the outermost gray cast iron parts during the test. The reason for this is likely the higher thickness of the outermost gray cast iron parts as discussed above. Other possible reasons could be variations in the material quality of the gray cast iron between the specimens, or that the slightly larger distance between the key holes in the current specimen (compared to the previously tested specimens) has a beneficial effect on the overall strain distribution.

In Figure 4.29 the measured ε_y at the ultimate tensile strength of the joint ($F_y = 193$ kN) is shown. Compared to the similar analysis of the symmetric joint (see Figure 4.16), the difference is that the largest tensile strains appear to be occurring in the area around the first heads of the shorter Metallock key components as opposed to the vicinity of the top heads of the outermost keyholes. During the test, it was also observed that the first failure of the gray cast iron component occurred at this location.

Since, in this case, there was no failure in the outermost parts of the gray cast iron component the strain distribution in Figure 4.29 should correspond to that of a Metallock

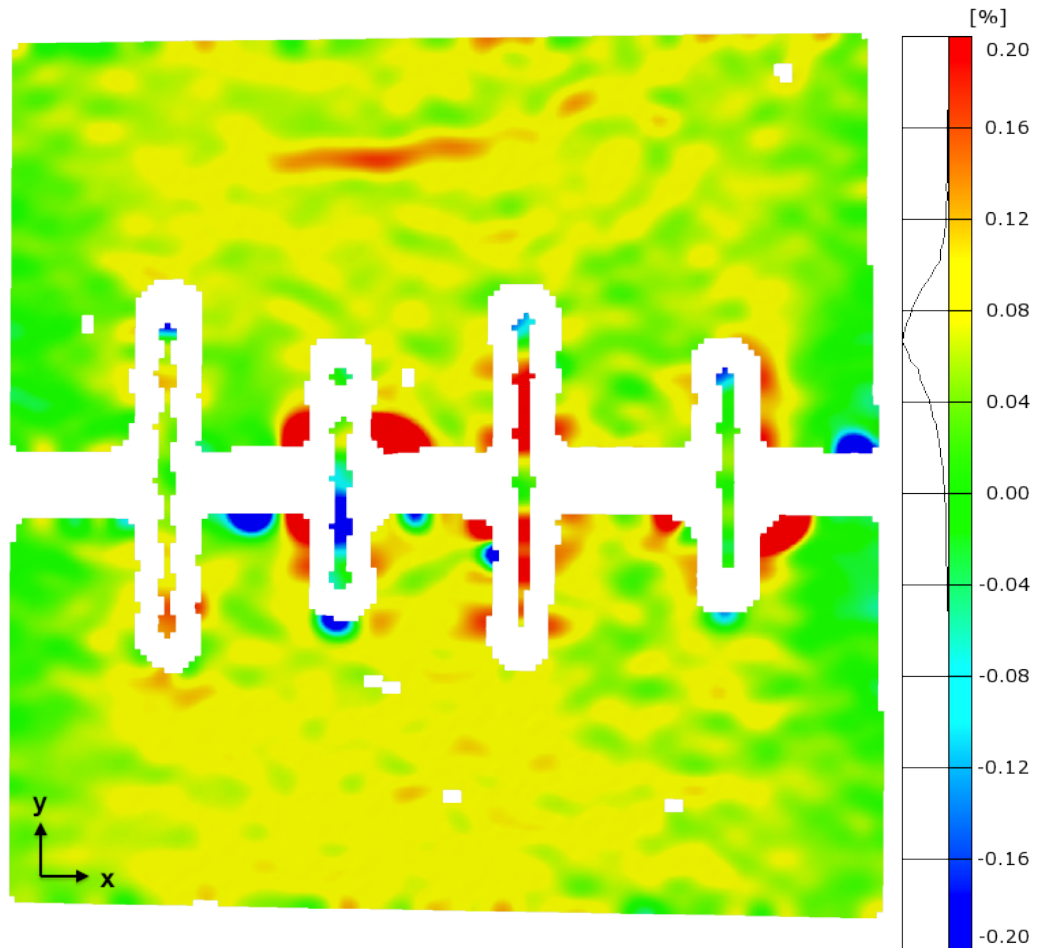


Figure 4.29: The measured ε_y at $F_y = 193$ kN.

joint less affected by boundary effects. Furthermore, the fact that the specimen failed in the area around the first heads of the shorter keys is in accordance with what has been measured and numerically predicted previously — namely that the keys distribute the load on all of their heads (however mostly on the head closest to the joint) and that longer keys therefore generate lower stresses in the gray cast iron material.

4.2.3 Joint with a 45° Inclination to the Load Direction

Joints with a 45° inclination to the load direction were subjected to loading in cyclic tension and cyclic compression, using large and small measurement volumes (see Appendix A). The results are presented in this section.

4.2.3.1 Cyclic Tension

In Figure 4.30, the global load versus displacement relation obtained using a virtual extensometer (in the same manner as described previously) on the specimen with a 45° inclination during cyclic tension. The relation does not seem to be initially linear as was observed in the corresponding plots for the straight specimens. The explanation to this could be that the initial deformation of the keys in this case depends on the bending stiffness rather than the tensile stiffness. Since the bending stiffness is lower than the tensile stiffness ($EI \ll EA$), the keys deform at a lower load when subjected to bending, see Figure 4.31.

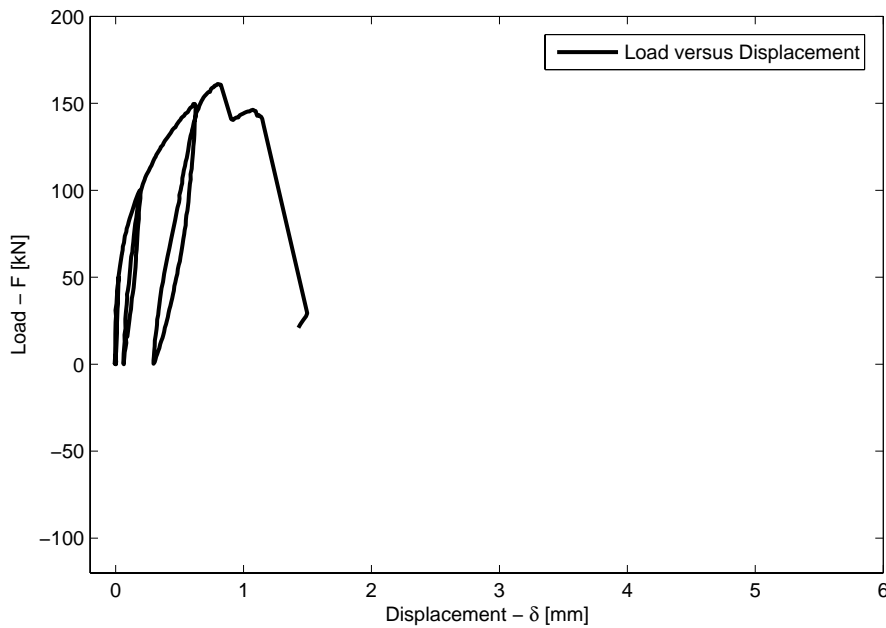


Figure 4.30: Measured global load–displacement relationship.

Comparing the behavior of the inclined joint to the corresponding behavior of the straight joints (see Figure 4.15, Figure 4.25, and Figure 4.28), it can be noted that for the inclined joint, as opposed to the straight joints, the “elastic modulus” seems to be decreasing with each load cycle, i.e. the slope of the elastic part is getting flatter for each load cycle.

At $F_y \approx 160$ kN, and $\delta_y \approx 0.8$ mm, the gray cast iron component failed at one of its outermost parts. After this, at $F_y \approx 150$ kN, and $\delta_y \approx 1.1$ mm, one of the gray cast iron components failed from a crack that was formed throughout the whole thickness of the specimen.

Figure 4.32 shows the measured ε_y distribution at the maximum load, $F_y = 161$ kN, in a specimen where the joint is inclined 45° to the load direction. The component failed in the right outermost gray cast iron part where also a propagation of strains from the lower key head to the edge of the specimen can be seen in Figure 4.32. Shortly after this, the upper gray cast iron part failed from a crack that was formed from right to left starting from one of the key heads, going towards the edge of the specimen.

Figure 4.33 shows the numerically predicted ε_{\max} strain field compared to the measured ε_{\max} strain field at $F_y = 61$ kN. In the numerical model (Figure 4.33a), the Metalock screws along the joint has been neglected and the large difference between the simulated and measured response is likely explained by this simplification. In the real specimen, most of the load at this load level is probably carried by the Metalock screws along the joint while in the numerical model, the Metalock keys are the only load carrying components which affect the strain field in the gray cast iron around the keys. This suggests that it is favorable with Metalock screw components along the joint if subjected to shear loading.

4.2.3.2 Cyclic Tension — Higher Resolution DIC Measurements

In Figure 4.34a, the measured maximum principal strain distribution of a part around three keys in the middle of the specimen is shown. It can be noted that there seems to be a concentration of strains in the centre of the keys. Figure 4.34b shows the distribution of strains along a section through the centre key in Figure 4.34a.

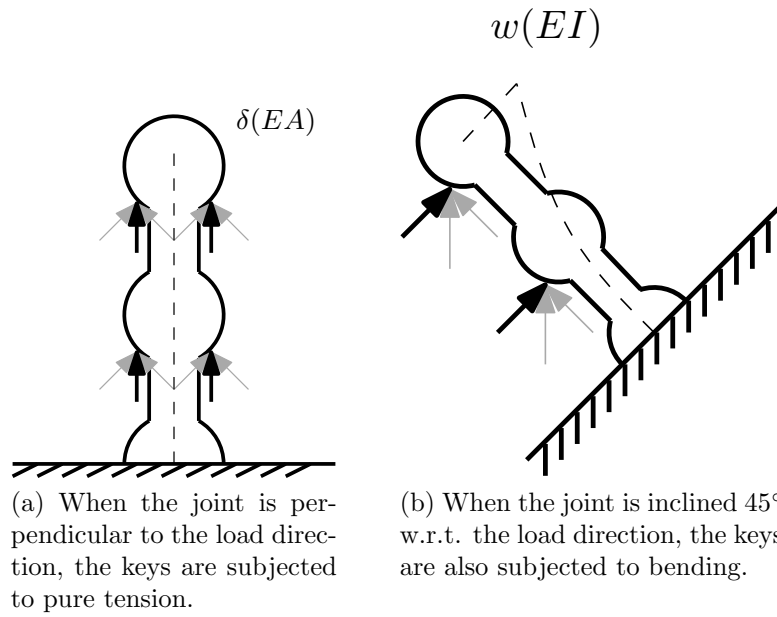


Figure 4.31: Difference in loading of (a) straight, and the (b) inclined specimens.

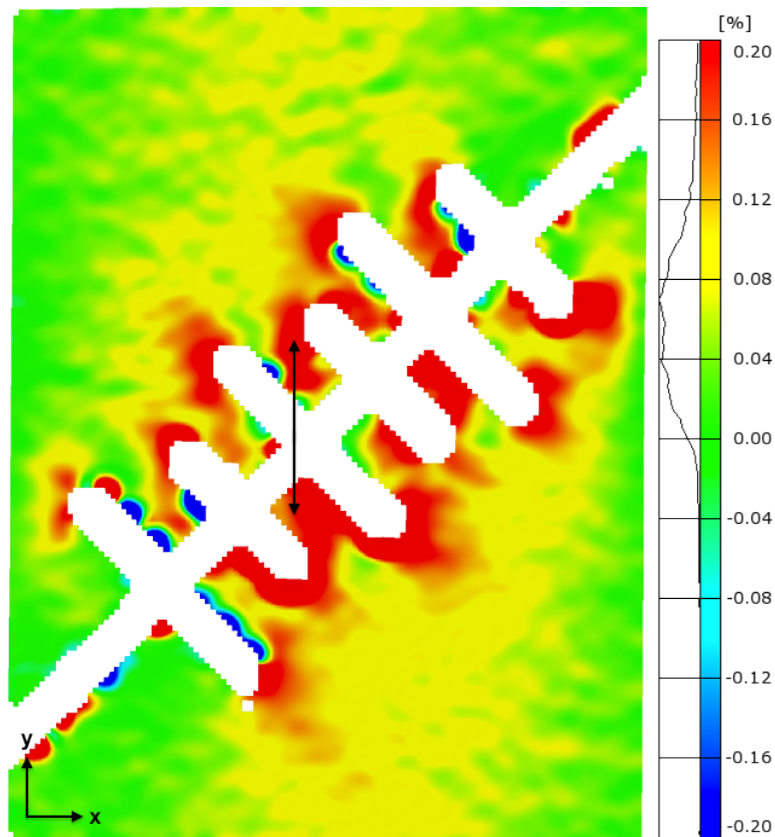


Figure 4.32: Measured ε_y distribution at $F_y = 161$ kN.

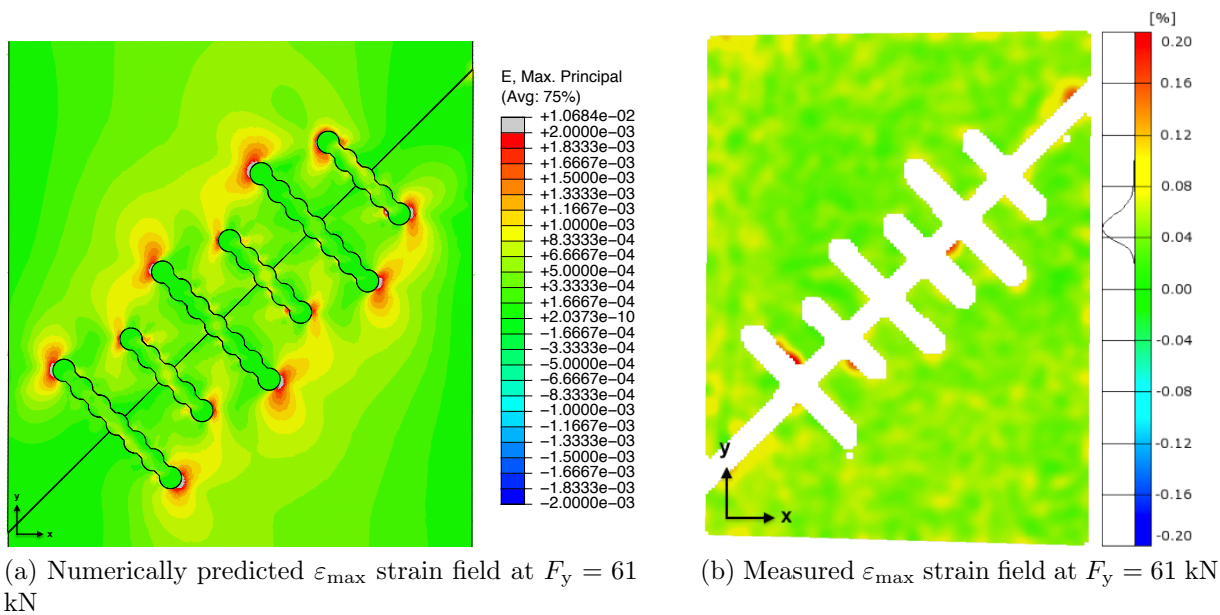


Figure 4.33: Comparison of the numerically predicted response to the measured response at $F_y = 61$ kN.

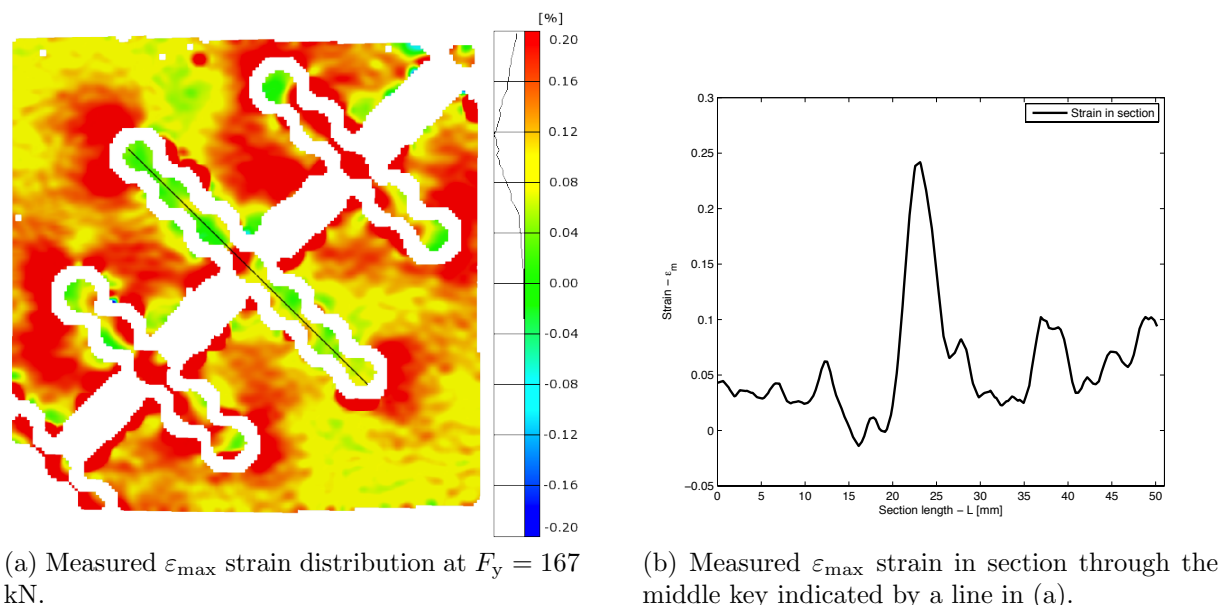
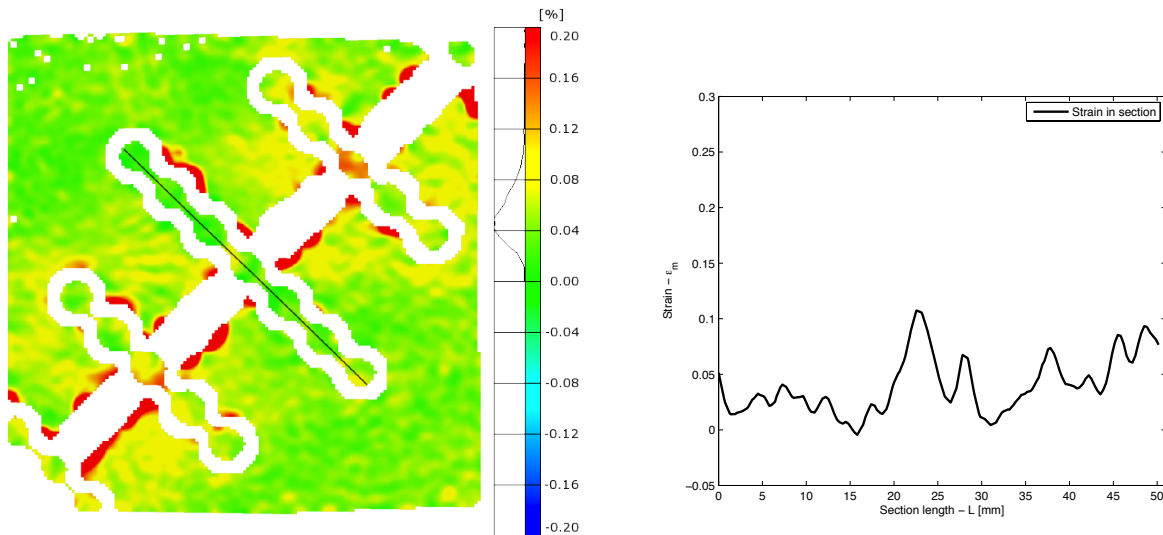


Figure 4.34: Measured ε_{\max} strain distribution and ε_{\max} strain-section coordinate at $F_y = 167$ kN.



(a) Measured ε_{\max} distribution at $F_y = 100$ kN.

(b) Measured ε_{\max} strain in a section through the centre key.

Figure 4.35: Measured ε_{\max} strain distribution and ε_{\max} strain–section length at $F_y = 100$ kN.

Figure 4.35 shows the corresponding measured maximum principal strain distribution at $F_y = 100$ kN. The same tendencies as at $F_y = 167$ kN can be observed, i.e. the largest strains in the keys occur in the centre.

4.2.3.3 Cyclic Compression

Figure 4.36 shows the measured global load–displacement relationship of a specimen where the joint has a 45° inclination to the load direction tested in compression. The relationship was measured in the same manner as in the previous tests. The original virtual extensometer length was $L \approx 61$ mm and the location can be seen in Figure 4.37.

Figure 4.37 shows the measured ε_y distribution at $F_y = -100$ kN. From what can be seen in the figure, there are no high strain fields at this load.

4.2.4 FEM Parametric Study

In this section the results from the parametric study of the influence of the key length and the distance between the key holes are presented.

4.2.4.1 Key Length

In Figure 4.38 and Figure 4.39, the numerically predicted locations of the maximum von Mises effective stress of the Metalock keys in the joint at $F_y = 100$ kN, with a standard key arrangement and the joint with longer keys are shown respectively. It seems as if the highest stresses occur in the first key layer and primarily at the first neck of the keys. The maximum value of von Mises effective stress differs between the two cases. In the case with the standard arrangement the maximum von Mises stress is $\sigma_{\text{vM}} = 738.8$ MPa, while in the case with the longer keys the maximum von Mises stress is $\sigma_{\text{vM}} = 692.7$ MPa. This means that the magnitude of the maximum von Mises effective stress is 7% larger in the case with the shorter keys which suggests that the joint with the longer keys has a slightly increased load carrying capacity.

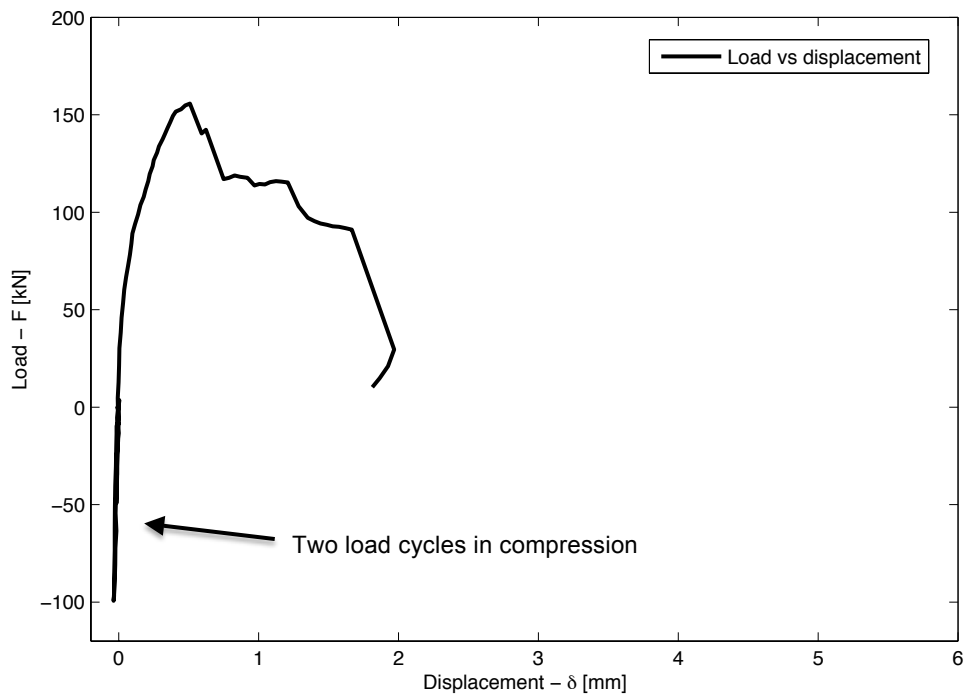


Figure 4.36: Measured global load-displacement relationship.

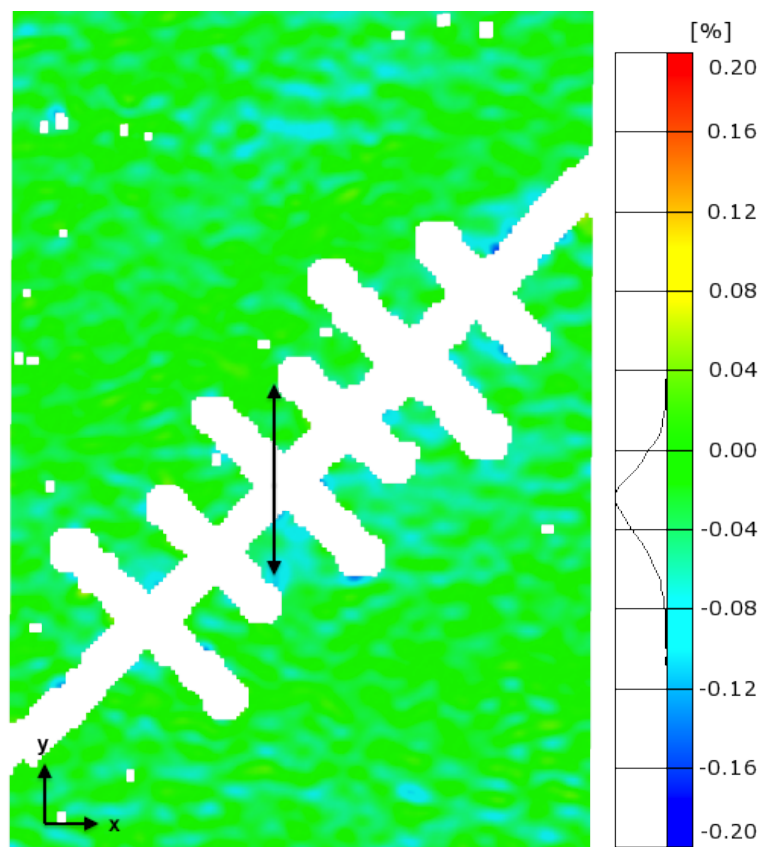


Figure 4.37: Measured ε_y distribution at $F_y = -100$ kN.

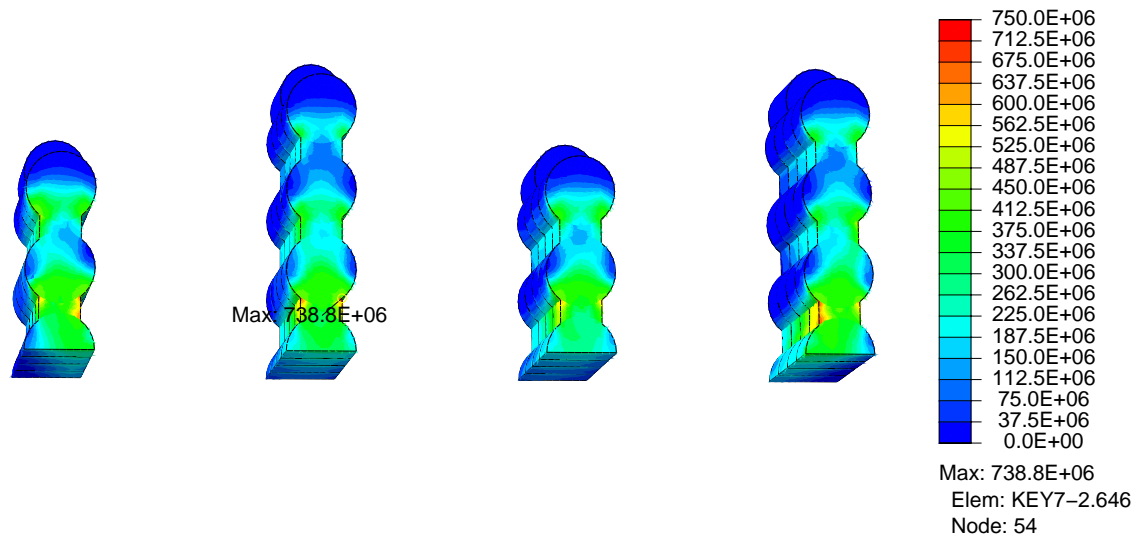


Figure 4.38: Numerically predicted location of the maximum von Mises effective stress at $F_y = 100$ kN in the joint with a 7-5-7-5 arrangement.

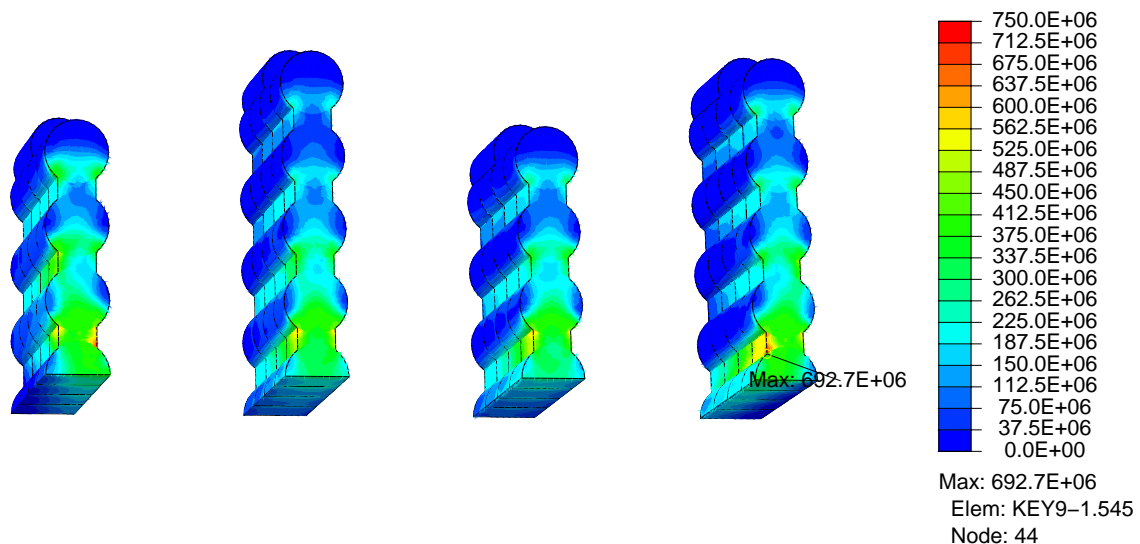


Figure 4.39: Numerically predicted location of the maximum von Mises effective stress at $F_y = 100$ kN in the joint with a 9-7-9-7 arrangement.

Figure 4.40 and Figure 4.41 show the numerically evaluated ε_y strain fields in the joints at $F_y = 100$ kN. The maximum ε_y occurs in the first key layer and in the first neck of the keys. The maximum value of the ε_y strain differs between the two cases — the strain is about 24% larger in the model with the standard key arrangement. Comparing Figure 4.40 to Figure 4.41, the concentrations of strains primarily in the top of the heads of the smaller keys seem to be less significant in the specimen with longer keys. However, in the gray cast iron, fields of ε_y strains of about $\varepsilon_y = 9 \cdot 10^{-4}$ appear to be connecting the top heads in the specimen with longer keys. This phenomenon is not as clearly apparent in the case with the standard key length arrangement.

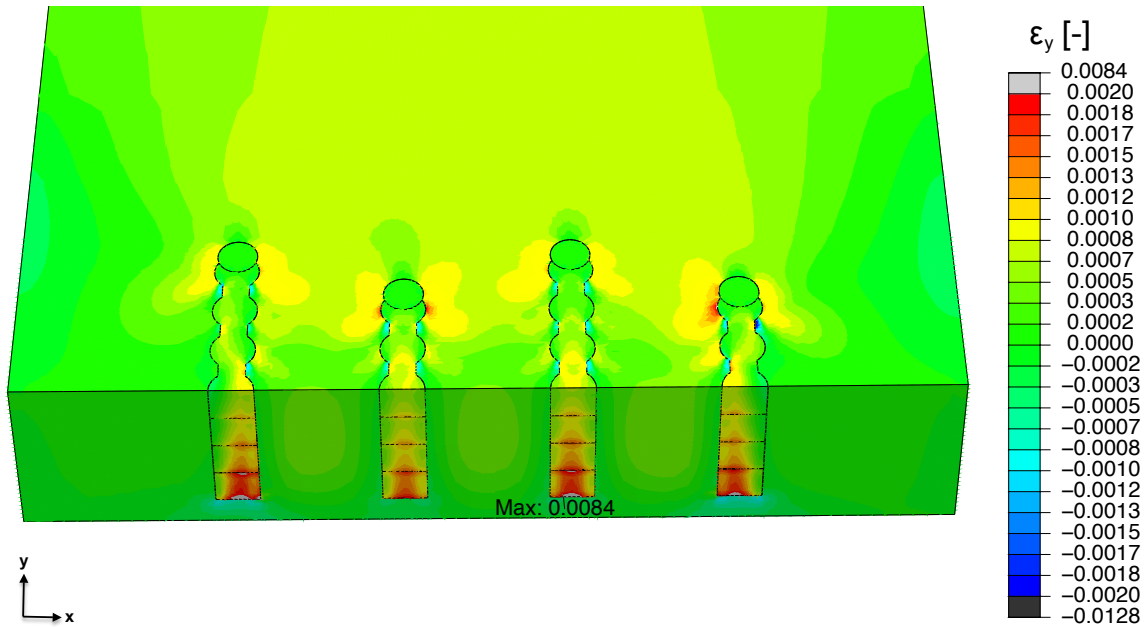


Figure 4.40: Numerically predicted ε_y strain field of the 7-5-7-5 joint.

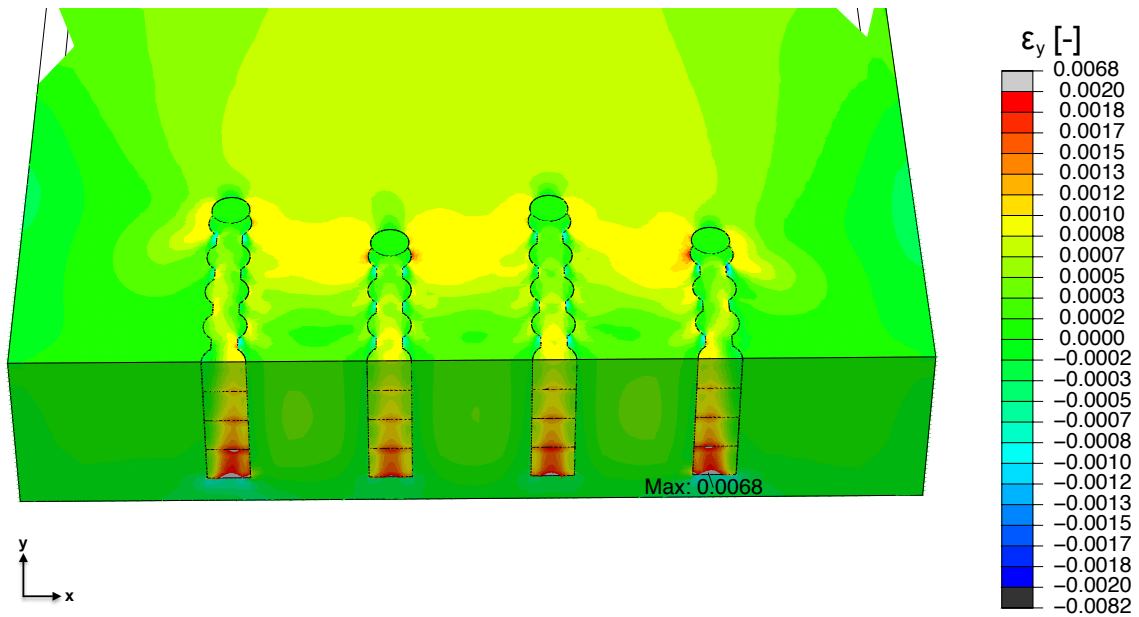


Figure 4.41: Numerically predicted ε_y strain field of the 9-7-9-7 joint.

In Figure 4.42 and Figure 4.43 numerically evaluated displacements, δ_y , at $F_y = 100$ kN, are shown. The maximum displacement occurs in the corner of each of the outermost keyholes in both of the models. It can be noted that in the model with longer keys, the maximum displacement is larger than the corresponding displacement in the standard joint. However, in both cases the maximum displacement is in the order of $\delta_y = 6 \cdot 10^{-5}$ m.

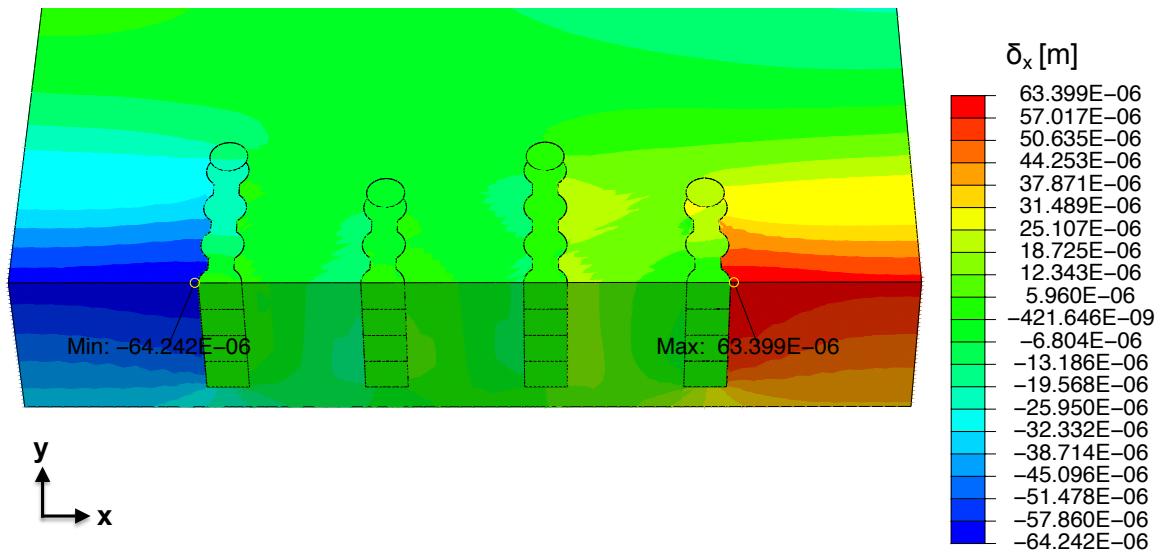


Figure 4.42: Numerically predicted displacement, δ_y , in the 7-5-7-5 joint [m].

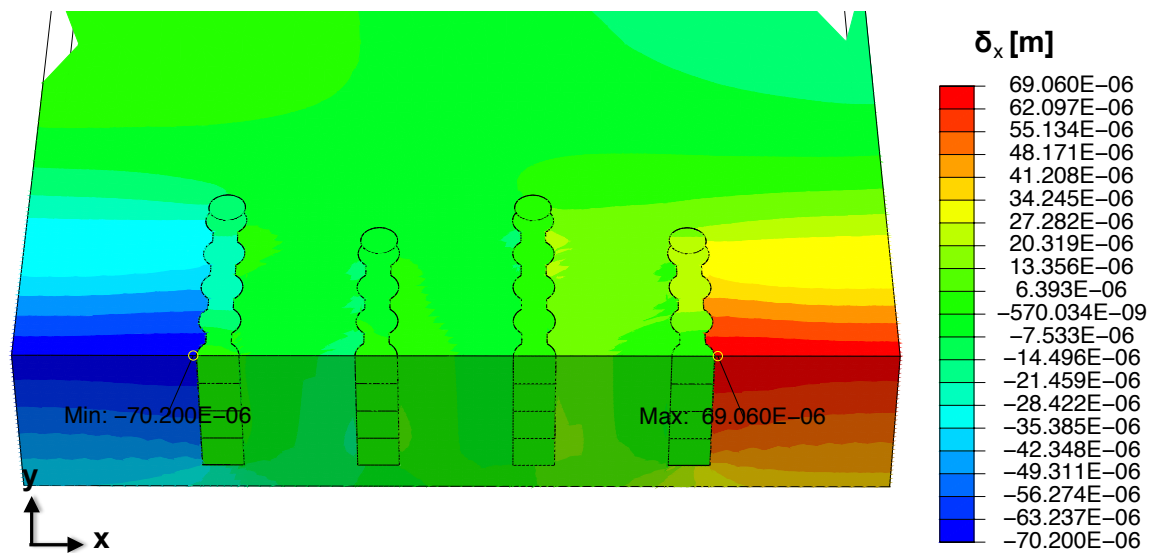


Figure 4.43: Numerically predicted displacement, δ_y , in the 9-7-9-7 joint [m].

4.2.4.2 Distance Between the Keyholes

Figure 4.44 and Figure 4.45 shows the ε_y strain fields at $F_y = 100$ kN in two models with 20 mm distance between the keyholes and 30 mm distance between the keyholes respectively. It is noticeable that the strain field seems to be more severe in Figure 4.44, i.e. in the model with smaller distance between the keyholes. It can also be noted that in the model with the shorter distance between the keys in Figure 4.44, there is a more pronounced field of strains in the gray cast iron between the top heads of each keyhole than what can be observed in the model with larger distance between the keyholes, see Figure 4.45. This indicates that cracking should initiate in this region at lower F_y loads if the distance between the keyholes is shorter.

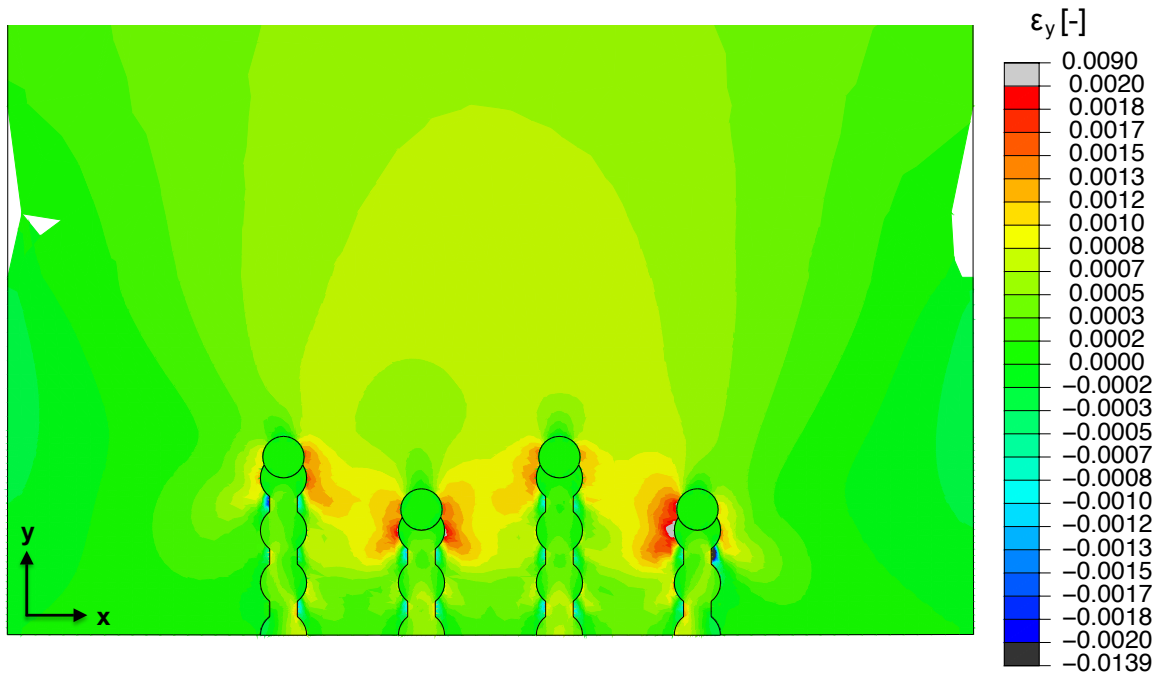


Figure 4.44: Numerically predicted ε_y strain field in a joint with 20 mm distance between the keyholes.

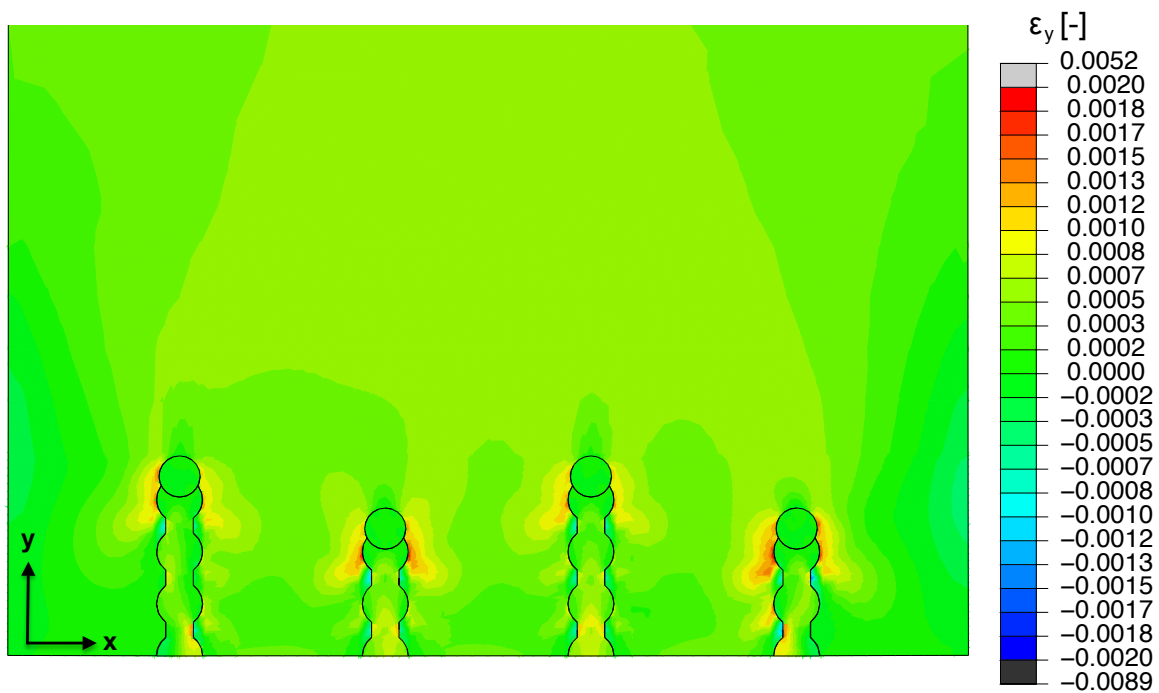


Figure 4.45: Numerically predicted ε_y strain field in a joint with 30 mm distance between the keyholes.

5 Conclusions

Regarding the physical properties of the Metalock keys, it can be concluded that they are made of an iron–nickel alloy with a composition not far from the common alloy Invar. The coefficient of thermal expansion is likely to be very low (or perhaps even negative in the temperature range $T = 30^{\circ}\text{C}$ to $T = 250^{\circ}\text{C}$), meaning that the Metalock keys will not expand in the same manner as the surrounding gray cast iron if subjected to thermal loading.

Hardness tests and microscopic analyses show that the Metalock keys have a varying hardness distribution along their length. This is most likely caused by cold working in the manufacturing process when forming the characteristic shape of the keys. The varying hardness distribution has an effect on the mechanical behavior of a joint when subjected to loading — it seems as if the magnitude of the strains along the keys are varying in a similar manner as the hardness.

The results of the experimental testing of Metalock joints indicate that the thickness of the material from the edge to the first keyhole is an important parameter regarding the load carrying capacity of the joint. If too thin, this outermost gray cast iron part becomes weak resulting in that the keys in the adjacent keyhole tend to be unable to function as load carrying elements.

Tests performed on specimens where the joint has a 45° inclination to the load direction indicate that deformation of the joint starts at lower tensile load levels than for specimens where the joint is perpendicular to the load direction, probably due to bending of the keys. Furthermore, Metalock screws are beneficial if a Metalock joint is subjected to shear loading.

Simulations show that the hammering treatment in the installation of the Metalock keys gives rise to residual strains primarily at the top of each keyhole in the gray cast iron material. Furthermore, experimental results give reason to believe that the residual strain magnitude is significant and it is considered likely that the impact is greatest on the top key layer, i.e. the keys at the surface of the joint.

Experimental testing and finite element simulations indicate that the length of the keys, i.e. the number of heads on each key, is an important parameter in the Metalock method, at least if the joint is perpendicular to the load direction. Simulations show that the load is primarily carried by the first head of each key, but also distributed to the other heads. This means that for longer keys the loading of the first head is decreased by distributing the load over a larger amount of heads than for the shorter keys.

Furthermore, the parametric finite element study shows that a larger distance between the keyholes has a beneficial effect on the strain distribution in the gray cast iron. If the keyholes are closely distanced, numerical simulations predict that strain fields form primarily between the top heads of the key components with magnitudes considerably higher than if the keyholes are more sparsely distanced.

References

- [1] Simulia. *Abaqus Analysis User's Manual*, 2010.
- [2] P.D. Webster. *Fundamentals of Foundry Technology*. Portcullis Press Limited, Redhill, 1st edition, 1980.
- [3] Metallnormcentralen. *Gjutlegeringar*. Stockholm, 2nd edition, 1978.
- [4] ASM International. *ASM Handbook*, 9th edition, 1992.
- [5] Serope Kalpakjian and Steven R. Schmid. *Manufacturing Processes for Engineering Materials*. Pearson Education, Inc., Upper Saddle River, 5th edition, 2008.
- [6] MAN Diesel. Man b&w material sheet no. p 607-3 for gray cast iron type c3cu, 2009.
- [7] ESAB. *Handbok för reparations- och underhållsvetsning*.
- [8] Metalock Engineering UK Ltd. Information brochure. <http://www.metalock.co.uk/>, 2008.
- [9] Michael A. Sutton, Jean-José Orteu, and Hubert W. Schreier. *Image Correlation for Shape, Motion and Deformation Measurements - Basic Concepts, Theory and Applications*. Springer Science+Business Media, New York, 1st edition, 2009.
- [10] Norman E. Dowling. *Mechanical Behavior of Materials: Engineering Methods for Deformation, Fracture, and Fatigue*. Pearson Education, Inc., Upper Saddle River, 3rd edition, 2007.
- [11] Simulia. *Getting Started with Abaqus - Interactive Edition*, 2007.
- [12] George E. Dieter. *Mechanical Metallurgy*. McGraw-Hill, Boston, 3rd edition, 1986.
- [13] Torsten Sjögren. Private communications, May 2011.
- [14] GOM. *Aramis User Manual - Software*, 2009.
- [15] Göran Grimvall. *Thermophysical properties of materials*. Elsevier, New York, 1999.

A DIC Test Setup

Table A.1: Overview of the different test setups.

Test no.	Joint type	Number of keys	Calibration volume [mm]	Load scheme
1	Straight	5	210 × 210	Cyclic tension
2	Straight	5	210 × 210	Cyclic compression
3	Straight	5	65 × 52	Cyclic tension
4	45° inclined	6	210 × 210	Cyclic tension
5	Straight	4	210 × 210	Cyclic tension
6	45° inclined	6	210 × 210	Cyclic compression
7	45° inclined	6	65 × 52	Cyclic tension
8	Straight	5	65 × 52	Cyclic tension

Table A.2: Post-processing parameters of the tests.

Test no.	Facet size [pixels]	Facet step [pixels]	Overlap [%]
1	15×15	13×13	13.3
2	15×15	13×13	13.3
3	12×12	9×9	25.0
4	13×13	11×11	15.4
5	10×10	9×9	10.0
6	10×10	9×9	10.0
7	15×15	13×13	13.3
8	15×15	13×13	13.3